Heliyon 10 (2024) e26010

Contents lists available at ScienceDirect

Heliyon

journal homepage: www.cell.com/heliyon

Research article

Investigation the effect of dissimilar laser welding parameters on temperature field, mechanical properties and fusion zone microstructure of inconel 600 and duplex 2205 stainless steel via response surface methodology

Ahmad Soleimani [a], Mohammad Akbari [a,b,*], Arash Karimipour [a,b], Amir Homayoon Meghdadi Isfahani [a,b], Reza Nosouhi [a,c]

[a] Department of Mechanical Engineering, Najafabad Branch, Islamic Azad University, Najafabad, Iran
[b] Aerospace and Energy Conversion Research Center, Najafabad Branch, Islamic Azad University, Najafabad, Iran
[c] Modern Manufacturing Technologies Research Center, Najafabad Branch, Islamic Azad University, Najafabad, Iran

ARTICLE INFO

Keywords:
Dissimilar laser welding
Inconel 600
Duplex 2205
Microstructural analysis
Response surface methodology
Mechanical properties

ABSTRACT

This study focused on dissimilar welding characterization of Inconel 600 and duplex 2205 stainless steel using central composite design (CCD) of experiments the response surface methodology (RSM). This study determined the effect of laser welding parameters and the reactions of the temperature field on the melt pool, the mechanical characteristics of the weld joint, and the geometry of the melt pool. According to the ANOVA results, the power of laser and focal distance were found to be the most influential factors on the temperature of both Inconel 600 and duplex stainless steel. The weld joint's tensile strength and elongation were significantly influenced by laser power and focal distance. Increasing the laser power from 250 to 450 W raised the tensile strength from 250 to 550 MPa. The Mo rich phases formed at the inter-dendritic region according to the EDS phase analysis results in loss of ductility and the resultant tensile strength of the samples failure from the fusion zone adjacent to the duplex stainless steel. At high laser power levels, the samples fractured from fusion zone while at lower laser powers below 350 W, the samples fractured from the HAZ and the areas adjacent to the duplex steel fusion line. The microhardness value of the weld joint at different laser power of 525 W and 375 W was increased to the maximum values of 370 and 325 HV, respectively from the fusion line of Inconel 600 to the center of the fusion zone. Further, molten pool microstructure of the dissimilar joint zone was mainly composed of a cellular and columnar dendritic structure Variations in melt flow, temperature gradient and solidification rate from the molten scan line to the weld center clearly changed the grain growth and the resultant microstructure in different areas of the fusion zone. By transferring the laser light to the center of the Inconel 600 and duplex stainless steel joint, the molten pool depth was increased from 0.2 to 1.5 mm.

* Corresponding author. Department of Mechanical Engineering, Najafabad Branch, Islamic Azad University, Najafabad, Iran.
E-mail address: m.akbari.g80@gmail.com (M. Akbari).

https://doi.org/10.1016/j.heliyon.2024.e26010
Received 31 October 2023; Received in revised form 21 December 2023; Accepted 6 February 2024
Available online 7 February 2024

1. Introduction

The development of experimental and numerical methods in manufacturing, material science, machining products and laser processing has revolutionized the way we process materials and manufacture products [1,2]. Among these methods, response surface methods and Analytic Network Process (ANP) can be mentioned [3]. The welding of dissimilar metals has been an interesting area of research due to the increased flexibility in the applications and design of the parts made in the production and industrial sectors [4,5]. However, the main challenge of joining dissimilar metals has been the differences in their physical and mechanical properties and chemical composition, thus making the precise selection of the welding process very important [6]. So far, many methods have been suggested for welding parts, one of the best of which is the use of high-power electron beams to connect parts. This method is also called radiant energy welding [7,8].

Inconel 600, which is an alloy with a high percentage of nickel, chromium and iron elements, is widely used in the aviation, chemical, and nuclear industries. Various parts made of this alloy are mostly used due to its high strength and corrosion resistance properties. It should be noted that the high amount of nickel and chromium, respectively, causes resistance to corrosion and oxidation of this alloy at high temperatures [9–12]. Duplex stainless steel, grade 2205 (DSS 2205), has equal proportions of ferritic and austenitic phases; equalization of phases causes high corrosion resistance, good toughness, and high mechanical strength due to the cheapness of this metal [13]. Welded joints between metals DSS 2205 and Inconel 600 are used in electronics, chemicals, aerospace, automotive, and other industries. Shielded metal arc (SMA), metal inert gas (MIG), and gas tungsten arc (GTA) are the common welding processes for joining dissimilar metals, DSS, and Ni-based superalloys. One of the major drawbacks of these processes is, however, the higher input heat, which causes such problems as liquid cracking, residual stress, distortion, micro-separation in the inter-dendritic distance, and lower welding scanning speed [14–17]. Inconel 625 and AISI 316 joints, using SMA and TIG welding processes, were analyzed by Kourdani et al. [18]. The results showed that a harmful phase of laves)intermetallic phases(was formed in the weld metal, and the resulting failure was due to the segregation of Nb. Devendranath Ramkumar et al. [19] also found that, in the non-homogeneous joints of DSS 2205 and Inconel 625, with the separation of Mo and Nb in the weld zone, due to the existence of secondary phases, the toughness and tensile strength of the weld joints were greatly reduced [20]. In the laser beam process, the higher welding speed at the high laser power generally ends in heating and therefore, fast cooling, leading to the reduction of elemental separation and the refinement of the microstructure [20,21]. Ramkumar et al. [22] also studied the parameters of laser power and laser welding speed of Inconel 718 and AISI 416 alloys; the results of micro-segregation and cracking in HAZ were reported. After laser welding of various alloys, including SUS 304 and Inconel 625, Li et al. [23] observed that the Mo and Nb elements were segregated, reducing the toughness and tensile strength. This micro-segregation was caused by the fast cooling rate. The results of another investigation conducted by Nawaz Ahmad et al. [24] on the welding of Inconel 625 and DSS 2205 also demonstrated that the microstructure was refined by speeding up the cooling process; niobium (Nb) and micro-segregation of molybdenum (Mo) in the inter-dendritic spacing were decreased, and the maximum tensile strength was achieved. Shamanian et al. also evaluated the heat input effect caused by laser welding on the mechanical properties, microstructure and penetration depth of the L-605 Co-based material. The input heat energy more than 48 J/mm resulted in the full penetration depth. The welded tensile strength was slightly higher or the same as that of a base metal [25].

Dissimilar pulsed laser welding of Inconel 600 and SS 304 was also conducted to investigate the weld bead surface and fusion zone microstructural characterization. The final weld zone microstructure, which included epitaxial growth, was generally composed of a dendritic and cellular microstructure, according to the solidification and temperature distribution contour of this region [26]. Yan et al. [27] also investigated the effects of laser welding variable parameters (welding scanning speed, laser power and nozzle distance) on the mechanical properties, microstructure and temperature distribution of the weld line of Inconel 625 and SS 304. It was found that the power of laser was the most effective parameter on the temperature and melting volume of Inconel 625, as compared to the austenitic stainless steel 304, which was clearly evaporated more, instead of melting, due to having a lower thermal conductivity rate.

This study experimentally investigated the effect of laser welding parameters on the temperature field near the dissimilar weld

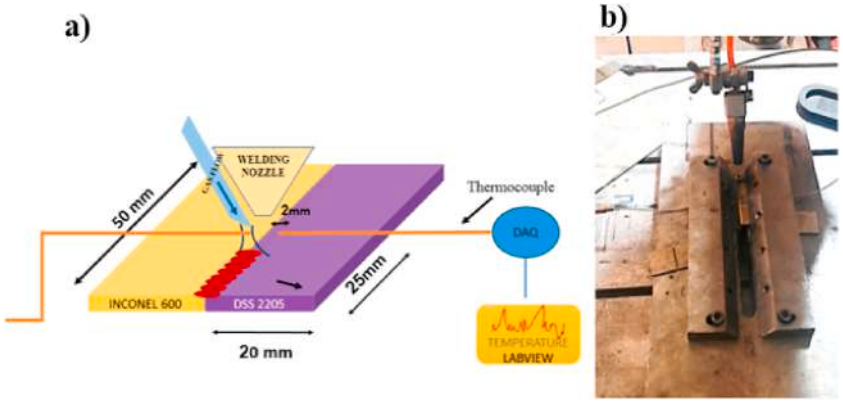

Fig. 1. Laser welding experimental setup, a) schematic, b) actual view.

fusion zone regions adjacent to the both base metals and thereby established a correlation between the laser welding parameters and microstructure of fusion zone, the contribution of each material to form the fusion zone and the impact of parameters on the mechanical properties of the dissimilar weld joint. According to the different thermomechanical properties of the both materials, selecting the appropriate parameters for dissimilar laser welding by considering different measurements based on the metallurgical, mechanical and thermophysical properties of both martials has been the main novelty of this work. It could be used in oil and gas storage containers and marine applications.

2. Material and methods

The fiber laser (Max Power = 500 W) with a continuous wave was used for laser welding experiments; it was equipped with Raytools head (BW210). The copper side nozzle was also used to protect the melt pool with the 1.5 lit/min pure argon gas flow rate. Every part of the workpiece made of different materials was prepared with 50x20 × 1.5 mm dimensions. For temperature measurement, the slot with 1 mm width and 0.8 mm depth was engraved by EDM to install thermocouples at the determined location. The K type thermocouple with the diameter of 1 mm was used for the temperature measurement range (−20 °C -400 °C with 1% accuracy). The temperature was measured at the center of workpiece and 2 mm distance from the center line of the molten zone, as illustrated in Fig. 1. To collect the thermocouples data, the analogue signal was transmitted through USB-4718 with 16-bit resolution, up to 0.1% input range accuracy or 4–20 mA inputs, to receive the temperature data and finally, recorded through the LABVIEW software.

Table 1 demonstrates the duplex stainless steel and Inconel 600 alloys' chemical composition. Laser welding experiments were carried out by fastening the workpieces and thermocouples on a special fixture. A 3-axis CNC table was then used to move the laser beam at the particular speed and position. The metallographic examinations from the cross section of dissimilar laser welded samples was performed according to the ASTME3 standard. The samples were mounted with the Bakelite powder at the press machine. The samples were then polished by 180–2000 grit sic paper and this was followed by polishing to prepare at a mirror-like condition to reveal the microstructure. The Olympus microscope, model BX51, was then implemented to take the microstructural images of the weld cross section. For the microstructural analysis of fusion zone and adjacent regions, FESEM TESCAN MIRA-3 was used. A ZWICK micro-hardness tester was subsequently used to measure microhardness at different regions of the weld cross section by utilizing the 100 g load at the dwell time of 12s. The welded samples tensile tests were prepared under the ASTME8 standard and the tensile test was conducted by using the GOTECH AI-7000 universal testing machine.

3. Design of experiments

For dissimilar laser welding of Inconel 600 alloy and duplex 2205, a set of primarily welding experiments was performed to evaluate the effect of laser welding parameters on the dissimilar welding efficiency by considering the volume of melting and formation of fusion zone on both metals. After visual investigation of the width and depth of the weld bead, the variables including laser power, focal distance, welding speed and deviation were selected at low and high level so as to create the weld bead at the joint area on both metals. The primarily set of experiments was observed in Table 2 in order to determine the levels limitation. A CCD experimental design including four main factors was followed to evaluate the effect of process variables on the responses by using RSM. The levels of factors can be observed in Table 3. Totally, 29 experiments composed of 5 central points, 16 points, and 8 axial points on the surfaces of a cube can be observed in Table 4. Generally, the design matrix has 28 degrees of freedom, including 18° for error, 14 for the Lack of fit, and 10 for the linear and non-linear terms. The higher degree of freedom for the error of regression model ensured the better accuracy of the test results. The nonlinear regression equation between the input parameters and the responses was then developed according to the RSM method. The target responses including the temperature near the fusion zone of both metals, tensile strength, the depth of the melt pool and elongation of the welded joint were considered as the responses.

4. Result and discussion

Dissimilar laser welding experiments was then conducted according to the RSM to systematically evaluate the effect of the welding parameters and their interactions on the responses. The variation of the responses, such as the temperature near the melt zone, during the process of welding of both base metals, by measuring the depth of the weld, the tensile strength and elongation rate, can determine the effectiveness of process parameters on the resultant weld quality through the analysis of variance (ANOVA). Seemingly, in other studies, experimental-numerical measurement of the temperature field during laser welding has been useful to determine the melting

Table 1
The alloys' chemical composition [28].

Element (W%)									
Alloy	Cu	Cr	Mn	Si	Fe	C	S	Ni	
INCONEL 600	0.1	15.5	0.25	0.2	8	0.05	0.002	Balance	
	Si	Mn	P	Al	Cr	Ni	Mo	S	C
Duplex 2205 steel	1	2.00	0.03	0.03	23	6.5	3.5	0.02	0.03

Table 2
Laser welding primarily experiments.

No.	Speed (mm/min)	Power (W)	Focal distance (mm)	Deviation (mm)	Heat input (kJ/mm)
1	200	450	0.0	0.0	0.135
2	200	300	0.0	0.0	0.088
3	200	450	5.0	−0.2	0.110
4	100	500	0.0	0.0	0.3
5	300	375	1.5	0.0	0.075
6	400	250	3.0	0.2	0.037

Table 3
The parameters variations in laser welding process.

No	Focal Distance (mm)	Speed (mm/min)	Power (W)	Deviation (mm)
1	−1.5- +4.5	200–400	200–450	−0.4-+0.4

Table 4
CCD matrix for laser welding experiments.

No.	Speed (mm/min)	Power (W)	Focal distance (mm)	Deviation (mm)	Heat input (kJ/mm)
1	200	450	0.0	0.2	0.135
2	200	450	3.0	0.2	0.122
3	400	450	0.0	−0.2	0.0675
4	400	300	0.0	−0.2	0.045
5	300	375	1.5	0.0	0.075
6	400	300	3.0	−0.2	0.041
7	300	375	1.5	0.0	0.075
8	300	375	4.5	0.0	0.068
9	400	300	0.0	0.2	0.045
10	300	375	1.5	0.0	0.075
11	400	450	3.0	−0.2	0.062
12	300	525	1.5	0.0	0.105
13	300	375	−1.5	0.0	0.075
14	500	375	1.5	0.0	0.045
15	400	450	0.0	0.2	0.0675
16	200	300	3.0	−0.2	0.082
17	100	375	1.5	0.0	0.225
18	300	375	1.5	0.4	0.075
19	200	450	0.0	−0.2	0.135
20	200	300	3.0	0.2	0.082
21	200	450	3.0	−0.2	0.123
22	300	225	1.5	0.0	0.045
23	200	300	0.0	−0.2	0.09
24	300	375	1.5	0.0	0.075
25	400	450	3.0	0.2	0.061
26	300	375	1.5	0.0	0.075
27	200	300	0.0	0.2	0.09
28	300	375	1.5	−0.4	0.075
29	400	300	3.0	0.2	0.041

efficiency of both metals, as reported before [29,30]. Therefore, by making a clear correlation between the temperature data for both metals, the weld geometry and microstructural changes could be gained according to the temperature gradient. Also, the weld joint mechanical properties could be altered by both the microstructure and melt pool geometry. Therefore, it could be said that taking the temperature as a dependent response can evidently determine the trend variation of other factors influenced by the temperature gradient. The regression equation can precisely predict the responses.

4.1. Evaluate of laser welding parameters on the temperature near melt zone

In dissimilar laser welding, different thermophysical properties have impact on equilibrium thermal conductivity when solid and liquid phases with different thermal conductivity, viscosity and melting points are fused simultaneously. The temperature measurement near the melt pool could indirectly determine the variation of the melting volume and the process of melting and solidification during welding.

4.1.1. Evaluate of laser parameters on the temperature variation around the Inconel 600 alloy

The temperature distribution according to the variation parameters for Inconel 600 was analyzed using ANOVA. The results are presented in Table 5. The values of Rsq 86.5% and lack of fit 0.482 showed that the model of regression had a good agreement with the experimental data. The laser power and focal distance were the most influential factors on the temperature of Inconel 600. The regression equation (1) shows a relation between process parameters including linear, square and the interaction and the temperature of Inconel 600.

$$\begin{aligned} Temperature\,(^{\circ}C) = & -209 + 1.162\,Power + 0.270\,Speed + 21.8\,Focal\,distance - 455\,Deviation - 6.01\,Focal\,distance * Focal\,distance \\ & - 385\,Deviation * Deviation - 0.00088\,Power * Speed - 0.0522\,Power * Focal\,distance + 0.500\,Power * Deviation \\ & + 0.0050\,Speed * Focal\,distance + 0.519\,Speed * Deviation + 22.1\,Focal\,distance * Deviation \end{aligned} \quad (1)$$

Fig. 2 evidently compares the laser power and focal distance parameters on the temperature changes of the Inconel 600 alloy. With increasing laser power, the temperature was raised by about 200 °C when the laser irradiated the more part of Inconel 600. The maximum temperature created at the focal distance of 2 mm was due to the creation of more melting volume across the molten pool and the laser beam approaching the location of the thermocouple temperature measurement, which caused an increase of temperature. By increasing the focal distance from 2 to 4 mm, due to the decrease of the energy density, the temperature created around the molten pool at the laser power of 450 W was diminished about 50 °C. Furthermore, it could be said that the variation of temperature at the higher laser power has been more highlighted, as compared to the lower level of laser power. The main reason could be a significant decrease in the melt volume created at the melt pool region at the higher laser power level; meanwhile, at laser power levels below 300 W, no notable changes in melt volume occurred during welding because of the insufficient laser power level for effective melting; therefore, temperature had no evident changes by increasing the focal distance. The maximum temperature generated at the 2 mm focal distance for the Inconel 600 alloy, by changing the power of laser scanning from 250 to 450 W, was about 200 °C; this was clearly seen because of creating more volume of melting, having enough level of laser beam energy density and the lower distance of the thermocouple tip from the laser beam. Therefore, the resultant temperature rise reached to the maximum value of 200 °C, as compared to the 0 mm distance that had the minimum beam diameter and higher distance from the thermocouple tip, and even 4 mm distance which had the minimum laser beam energy density and the lower melting efficiency among all.

Fig. 3 shows the effect of beam deflection and laser power on the temperature changes of Inconel 600 alloy. By increasing the laser power from 250 W to 450 W, the temperature of Inconel 600 was increased by about 80 °C.

On the other hand, it could be seen that the deviation of the laser beam, as compared to the laser power, did not have a remarkable effect on the temperature changes of the Inconel 600 alloy. The center of the intersection of the two sections generated the highest temperature during the laser beam's radiation. It was clear that the influence of laser power on temperature variations followed a nearly identical pattern. Although there was not a significant difference in the melting points of the two metals, the temperature was decreased with the laser beam's deviation towards the Inconel 600 alloy (−0.5 mm) due to the melting volume reduction in the formation of the molten pool and the lower laser beam absorption rate.

Fig. 4 shows the laser power and welding speed effects on the temperature changes beside the fusion zone of the Inconel 600 alloy. The temperature around the molten pool was linearly increased from 100 °C to 300 °C by changing the laser power from 200 to 450 W. It could be seen that the changes in the welding speed, as compared to the those in the power of laser, did not have a significant effect

Table 5
ANOVA results for the temperature of Inconel 600.

Source	DF	Adj SS	Adj MS	F-Value	P-Value
Model	12	123004	10250.3	8.60	0.000
Linear	4	108195	27048.9	22.71	0.000
Power (W)	1	90528	90528.2	76.00	0.000
Speed (mm/min)	1	683	682.7	0.57	0.460
Focal distance (mm)	1	11094	11094.0	9.31	0.008
Deviation (mm)	1	5891	5890.7	4.95	0.041
Square	2	10220	5110.1	4.29	0.032
Focal distance (mm)*Focal distance (mm)	1	5055	5054.9	4.24	0.056
Deviation (mm)*Deviation (mm)	1	6553	6552.8	5.50	0.032
2-Way Interaction	6	4588	764.7	0.64	0.696
Power (W)*Speed (mm/min)	1	702	702.2	0.59	0.454
Power (W)*Focal distance (mm)	1	552	552.2	0.46	0.506
Power (W)*Deviation (mm)	1	900	900.0	0.76	0.398
Speed (mm/min)*Focal distance (mm)	1	9	9.0	0.01	0.932
Speed (mm/min)*Deviation (mm)	1	1722	1722.3	1.45	0.247
Focal distance (mm)*Deviation (mm)	1	702	702.2	0.59	0.454
Error	16	19059	1191.2		
Lack-of-Fit	12	14836	1236.3	1.17	0.482
Pure Error	4	4223	1055.8		
Total	28	142063			
S R-sq (pred) R-sq (adj) R-sq					
34.5139 50.55% 76.52% 86.58%					

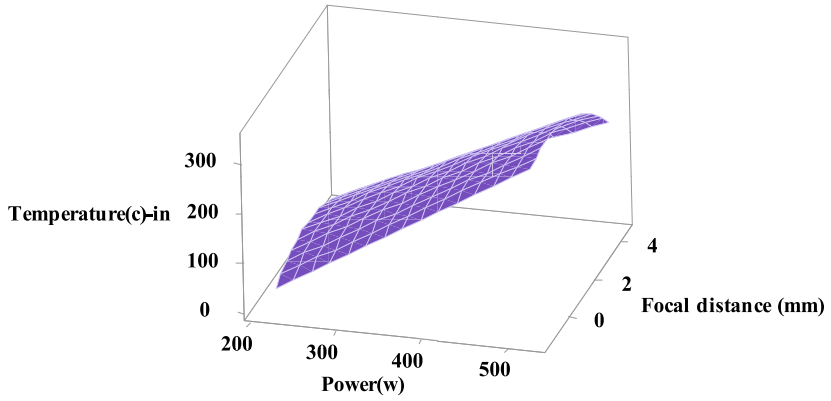

Fig. 2. Evaluate laser power and focal distance changes on the temperature at 2 mm distance from the center of melt zone for Inconel 600 alloy.

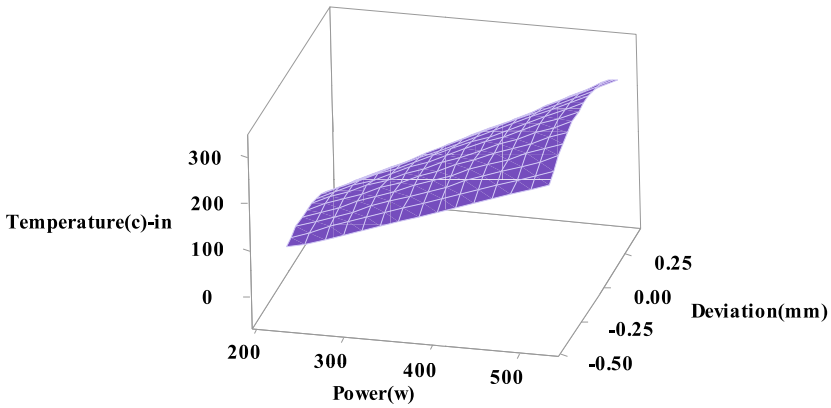

Fig. 3. Effects of laser beam deviation and laser power on the temperature at distance of 2 mm from the center of fusion zone for Inconel 600 alloy.

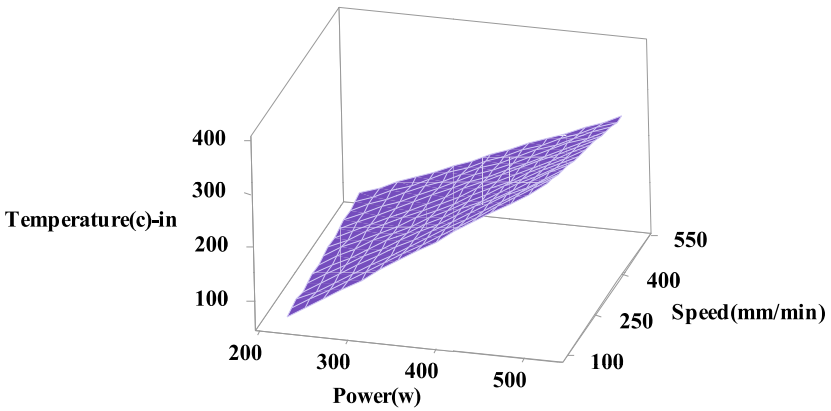

Fig. 4. Analyze the welding speed and laser power effect on the temperature at distance of 2 mm from the center of melt pool for Inconel 600 alloy.

on the temperature changes of the Inconel 600 alloy. However, with the increase in the speed of welding, a decrease of temperature could be partially observed. The rate of temperature increase at a lower speed was due to the creation of a larger melting volume and a longer duration of the laser beam interaction with the work piece. The effect of laser power at a level more than 400 W experienced more reduction due to decreasing the melt volume, according to the lower laser material interaction time and absorbsion rate.

Table 6
ANOVA results for the temperature changes beside the fusion zone of duplex stainless steel.

Source	DF	Adj SS	Adj MS		F-Value	P-Value
Model	12	119296	9941.3		23.02	0.000
Linear	4	80301	20075.2		46.48	0.000
Power (W)	1	74148	74148.2	171.68		0.000
Speed (mm/min)	1	2604	2604.2	6.03		0.026
Focal distance (mm)	1	1980	1980.2	4.58		0.048
Deviation (mm)	1	1568	1568.2	3.63		0.075
Square	2	23327	11663.5	27.00		0.000
Focal distance (mm)*Focal distance (mm)	1	22219	22219.3	51.44		0.000
Deviation (mm)*Deviation (mm)	1	156	156.5	0.36		0.556
2-Way Interaction	6	15668	2611.3	6.05		0.002
Power (W)*Speed (mm/min)	1	2704	2704.0	6.26		0.024
Power (W)*Focal distance (mm)	1	1	1.0	0.00		0.962
Power (W)*Deviation (mm)	1	3600	3600.0	8.34		0.011
Speed (mm/min)*Focal distance (mm)	1	8281	8281.0	19.17		0.000
Speed (mm/min)*Deviation (mm)	1	121	121.0	0.28		0.604
Focal distance (mm)*Deviation (mm)	1	961	961.0	2.23		0.155
Error	16	6910	431.9			
Lack-of-Fit	12	5834	486.2	1.81		0.299
Pure Error	4	1076	269.0			
Total	28	126206				
S R-sq R-sq (adj) R-sq (pred)						
20.7823 94.52% 90.42% 78.34%						

4.1.2. Analyzing the laser parameters variations on the temperature changes beside the duplex 2205

Table 6 displays the results of ANOVA for the temperature near the Fusion zone on DSS. It is clear from the lack of fit, which was 0.299, and Rsq, which was 94.5%, that the regression model and experimental data were in a good agreement. The power of laser and welding speed of linear term and the interaction between the welding speed and focal distance were the most influential factors on the temperature changes of DSS 2205. The regression equation (2) depicts a relation between process parameters including linear, square and interaction and the temperature of duplex 2205.

$$\begin{aligned}\text{Temperature } (^{\circ}\text{C}) = & -301.6 + 1.264\ \text{Power} + 0.773\ \text{Speed} + 78.1\ \text{Focal distance} - 337\ \text{Deviation} - 12.61\ \text{Focal distance} \\ & * \text{Focal distance} + 59.5\ \text{Deviation} * \text{Deviation} - 0.001733\ \text{Power} * \text{Speed} - 0.0022\ \text{Power} * \text{Focal distance} + 1.000\ \text{Power} \\ & * \text{Deviation} - 0.1517\ \text{Speed} * \text{Focal distance} + 0.138\ \text{Speed} * \text{Deviation} - 25.8\ \text{Focal distance} * \text{Deviation} \end{aligned} \quad (2)$$

The effect of the distance of focal and beam deviation on the temperature of duplex steel can be seen in Fig. 5. The temperature measured by thermocouples was always increased with the deviation of the laser beam towards the DSS. At the same time, the laser beam was transmitted to the value of 0.2 mm on the side of duplex steel. There was also an increase in the fusion volume and temperature of DSS. In addition to these, the laser beam got closer to the thermocouple tip, as compared to the previous location. The maximum amount of temperature was at the focal distance of 2 mm; with further increase of the focal distance, the temperature changes beside the fusion zone decreased because of having lower energy density and lower melt volume, although the laser beam got

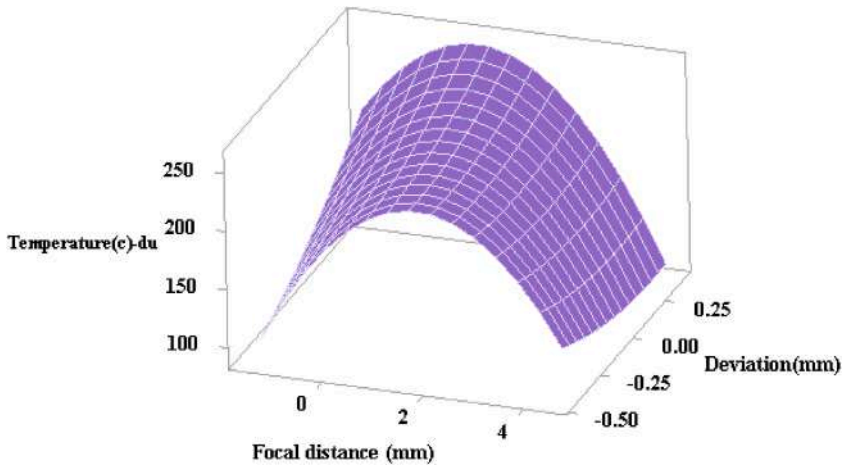

Fig. 5. The effect of focal distance and laser beam deviation on the temperature changes at the 2 mm distance from the center of melt area for duplex 2205.

closer to the thermocouple tip. The transfer of the laser beam to the alloy 600 reduced the temperature of the duplex steel by about 60 °C due to the more distance of the highest energy of laser beam position from the thermocouple tip.

Fig. 6 shows the effect of laser power and focal distance on the duplex steel temperature. With increasing laser power, a temperature increase of about 100 °C was observed at different focal distances. The maximum temperature created at a focal distance of 2 mm was at a power of 450 W. In the focal distance of 2 mm and laser power level of 450 W, the maximum temperature around the molten pool was observed to be around 310 °C. It could be, therefore, said that at this point, the melting volume was increased significantly because of having enough laser beam energy density to fully penetrate along the workpiece thickness; also, the bigger width of the melt area has clearly augmented the fusion volume and the resultant measured temperature during the laser welding process.

Fig. 7 shows the effect of welding speed and laser power on the temperature of DSS. By increasing the laser power from 250 to 450 W, the temperature of duplex steel was raised by about 200 °C at the scanning speed of 200 mm/min. In case the laser welding speed was raised up to 500 °C, the increase rate was about 120 °C. Therefore, it could be said that increasing the welding speed reduced the temperature by about 25%. The temperature was raised at the speed of 200 mm/min about 200 °C, which was the highest increase rate among other parameters. On the other hand, it was clear that with the increase of the welding scanning speed, the temperature of duplex steel was decreased by about 50 °C when the laser power was at the level of 450 W. At the laser power of 200 W, no evident reduction was observed with the increase of the welding scanning speed because of insufficient melting volume and low laser line energy. Hence, incomplete melt volume at a laser power level below 300w did not alter the temperature gradient and therefore, melting efficiency of the weld conjunction.

4.1.3. How laser parameters affect the melt pool's depth

Table 7 presents the ANOVA findings for the molten pool depth, revealing that the molten pool depth was mostly affected by two variables: laser power and welding speed. The regression model values of Rsq = 95.69% and Lack of Fit = 0.412 demonstrate how well they could be matched with the experimental data. Linear, quadratic, and non-linear components on the interaction of parameters are also included in equation of regression (3) for the depth of the fusion area.

$$\begin{gathered} Depth\ (mm) = -0.303 + 0.004511\ Power\ -\ 0.001517\ Speed + 0.0096\ Focal\ distance + \\ 3.035\ Deviation - \ 0.00580\ Focal\ distance\ *\ Focal\ distance + 0.143\ Deviation * Deviation\ -\ 0.00592\ Power * Deviation \\ - 0.000117\ Speed * Focal\ distance\ -\ 0.00212\ Speed * Deviation + \\ 0.1083\ Focal\ distance\ * Deviation \end{gathered} \tag{3}$$

Fig. 8 depicts the impact of laser power and laser beam deviation on the depth of the fusion area. As the laser power was increased, the depth of the molten zone was raised. On the other hand, it could be seen that the molten zone depth had lower variation with the laser beam deviation towards the duplex steel. It could be, therefore, said that at the 200 W laser power, by deflecting the laser beam towards the Inconel 600 super alloy, due to its lower absorption coefficient, as compared to duplex steel, a smaller melting volume was created. By transferring the laser light to the center of the Inconel600 joint and duplex stainless steel, the molten pool depth was increased from 0.2 to 1.5 mm. Therefore, with the higher absorption rate of the laser beam by duplex steel, the melting volume was clearly increased, although the major part of the melted material was composed of the melting Inconel 600 due to heat conduction from the duplex stainless steel. It could be, therefore, said that the mechanism of the melt pool formation would have been through both direct laser beam penetrations toward Inconel 600 and the other one from the heat conduction from DSS.

Fig. 9 depicts the effect of welding speed and laser beam deflection on the depth of the molten area. It is clear that the maximum rate of decrease in the depth of the fusion area was when the laser beam was deflected on the duplex steel. By increasing the welding speed from 200 mm/min to 450 mm/min, the depth of the molten pool was decreased by about 1 mm. In general, the molten pool's

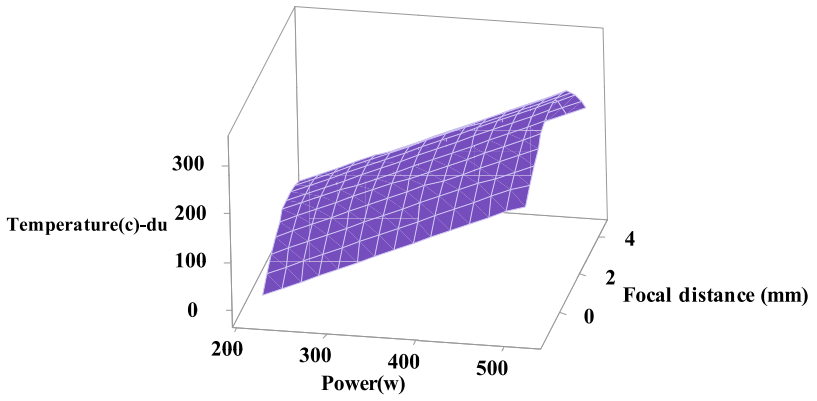

Fig. 6. The evaluation of changes for focal distance and laser power on the temperature at 2 mm distance from the center of melt area for duplex 2205.

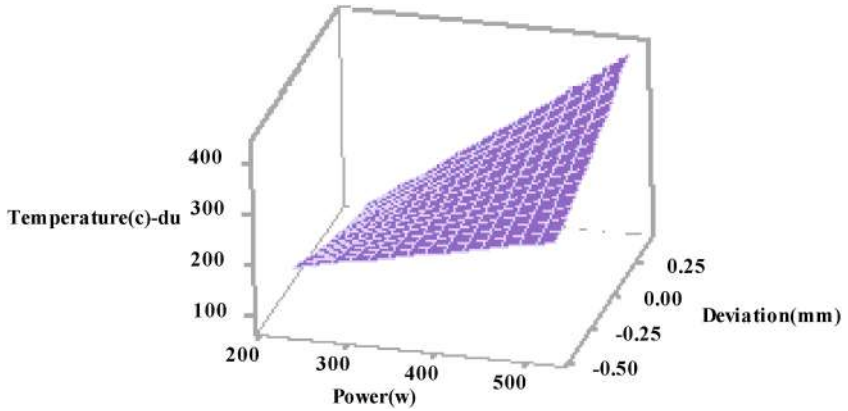

Fig. 7. The impact of beam deviation and laser power on temperature at the 2 mm distance from the melt zone's center for duplex 2205.

Table 7
ANOVA results for depth of the melt pool.

Source	DF	Adj SS	Adj MS	F-Value	P-Value
Linear	4	3.64497	0.91124	95.08	0.000
Model	10	3.82797	0.38280	39.94	0.000
Power (W)	1	2.74727	2.74727	286.65	0.000
Speed(mm/min)	1	0.68682	0.68682	71.66	0.000
Focal distance (mm)	1	0.09882	0.09882	10.31	0.005
Deviation (mm)	1	0.11207	0.11207	11.69	0.003
Square	2	0.00628	0.00314	0.33	0.725
Focal distance (mm)*Focal distance (mm)	1	0.00469	0.00469	0.49	0.493
Deviation (mm)*Deviation (mm)	1	0.00090	0.00090	0.09	0.763
2-Way Interaction	4	0.17672	0.04418	4.61	0.010
Power (W)*Deviation (mm)	1	0.12602	0.12602	13.15	0.002
Speed (mm/min)*Focal distance (mm)	1	0.00490	0.00490	0.51	0.484
Speed (mm/min)*Deviation (mm)	1	0.02890	0.02890	3.02	0.100
Focal distance (mm)*Deviation (mm)	1	0.01690	0.01690	1.76	0.201
Error	18	0.17251	0.00958		
Lack-of-Fit	14	0.14283	0.01020	1.37	0.412
Pure Error	4	0.02968	0.00742		
Total	28	4.00048			
S R-sq R-sq (adj) R-sq (pred)					
0.0978985 95.69% 93.29% 86.99%					

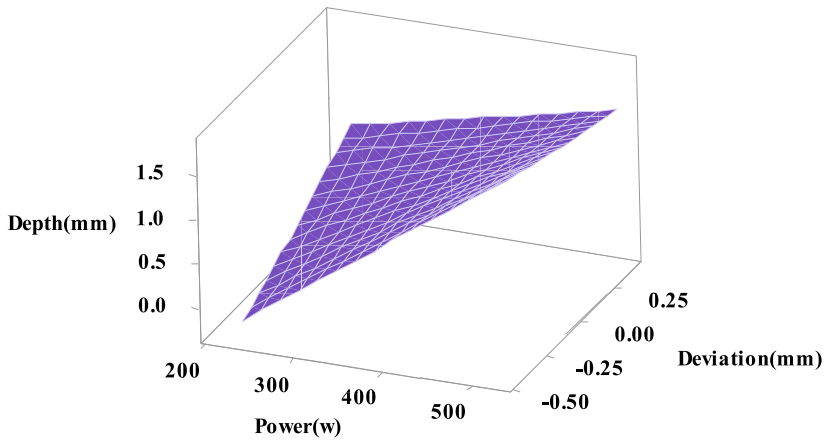

Fig. 8. The impact of beam deviation and laser power on depth of the melt pool.

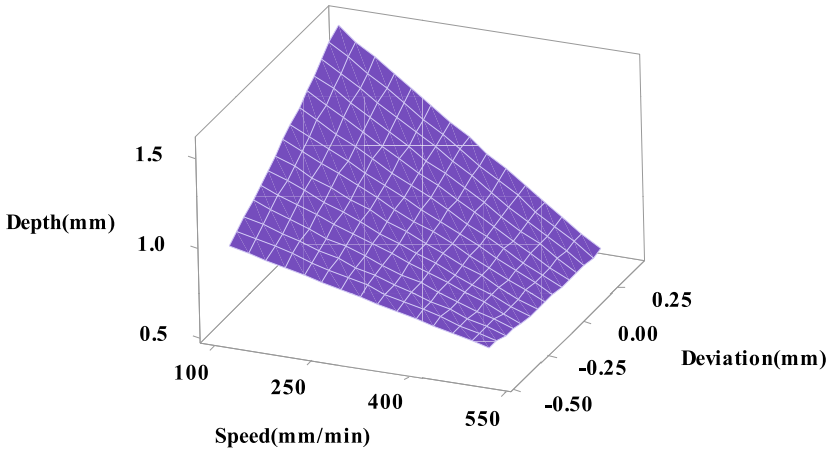

Fig. 9. The impact of welding scanning speed and laser beam deviation on depth of the melt pool.

depth was raised by 0.8 mm as a result of the laser beams with the speed of 200 mm/min deflection towards the duplex steel. As can be seen, the depth of the fusion area did not change much with the displacement of the laser beam at a speed of 450 mm/min due to the short laser beam interaction time with the metal material and insufficient melting.

Furthermore, by increasing the welding speed in case the laser beam deviated toward Inconel 600 alloy, the created melt pool depth was about half of that the position of duplex steel. Also, the rate of depth variation by the welding speed was significantly lower when the laser beam deviated on Inconel 600.

Fig. 10 depicts the impact of the focal distance and laser beam deviation on the depth of the molten pool. By increasing the parameters of focal distance when irradiating the laser beam towards the Inconel 600 alloy, the molten zone depth was raised about 0.6 mm. Also, the depth reduction rate of the fusion area was the highest at the focal distance of 4 mm. By performing the welding process at the focal point, due to the high energy density of the laser beam, the depth of the molten pool did not change much and the laser beam penetrated almost to the maximum depth of the thickness of the part. By increasing the focal distance, especially the laser beam deviation towards the Inconel 600, the molten area depth was decreased about 50%. This was because of laser energy density reduction and the lower absorption rate by Inconel 600, thereby creating the lower melt volume.

The maximum molten zone depth was created at the focal distance of 2 mm, when the beam of laser was irradiated on the DSS. In this case, both laser penetration and melting volume have enough values to increase the melt area depth.

4.1.4. The impact of laser parameters changes on the weld joint tensile strength

As can be observed in Table 8, according to the ANOVA results, two parameters of laser power and focal distance had a great influence on welded samples' tensile strength. The laser power and focal distance clearly had impact on the melt zone depth and melt volume at the fusion zone, which could directly influence the tensile strength of the welded sample. The regression equation (4) represents the relation between the input parameters of laser welding and tensile strength.

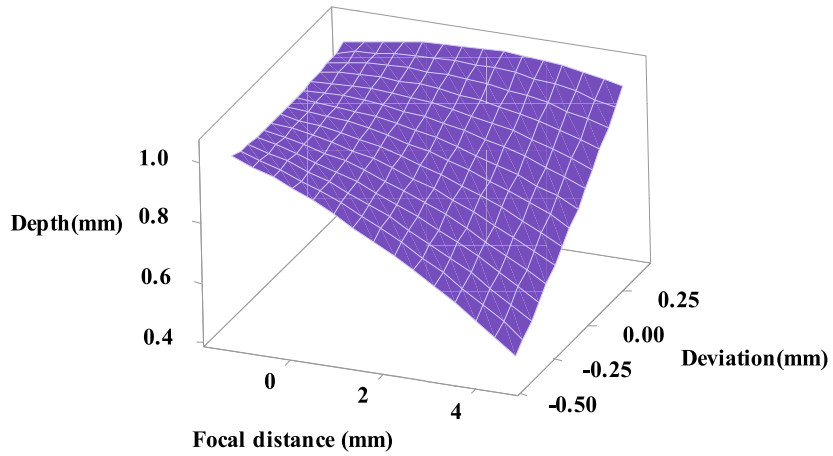

Fig. 10. The impact of focal distance and laser beam deviation on the melt zone depth.

Table 8
ANOVA results for weld section tensile strength.

Source	DF	Adj SS	Adj MS	F-Value	P-Value
Model	14	272336	19453	17.49	0.000
Linear	4	221491	55373	49.79	0.000
Power (W)	1	193860	193860	174.32	0.000
Speed (mm/min)	1	4455	4455	4.01	0.065
Focal distance (mm)	1	20592	20592	18.52	0.001
Deviation (mm)	1	2583	2583	2.32	0.150
Square	4	32043	8011	7.20	0.002
Power (W)*Power (W)	1	26303	26303	23.65	0.000
Speed (mm/min)*Speed (mm/min)	1	6205	6205	5.58	0.033
Focal distance (mm)*Focal distance (mm)	1	311	311	0.28	0.605
Deviation (mm)*Deviation (mm)	1	259	259	0.23	0.637
2-Way Interaction	6	18802	3134	2.82	0.052
Power (W)*Speed (mm/min)	1	4590	4590	4.13	0.062
Power (W)*Focal distance (mm)	1	13168	13168	11.84	0.004
Power (W)*Deviation(mm)	1	431	431	0.39	0.544
Speed (mm/min)*Focal distance (mm)	1	248	248	0.22	0.644
Speed (mm/min)*Deviation (mm)	1	352	352	0.32	0.583
Focal distance (mm)*Deviation (mm)	1	14	14	0.01	0.912
Error	14	15570	1112		
Lack-of-Fit	10	14100	1410	3.84	0.103
Pure Error	4	1469	367		
Total	28	287906			
S R-sq R-sq (adj) R-sq (pred)					
33.3484 94.59% 89.18% 70.99%					

$$\text{Tensile strength (Mpa)} = 429 - 1.987\,\text{Power} - 0.257\,\text{Speed} + 63.6\,\text{Focal distance} + 3\,\text{Deviation} + 0.00566\,\text{Power} * \text{Power} + 0.001546\,\text{Speed} * \text{Speed} + 1.54\,\text{Focal distance} * \text{Focal distance} - 79\,\text{Deviation} * \text{Deviation} - 0.00226\,\text{Power} * \text{Speed} - 0.2550\,\text{Power} * \text{Focal distance} - 0.346\,\text{Power} * \text{Deviation} + 0.0262\,\text{Speed} * \text{Focal distance} + 0.234\,\text{Speed} * \text{Deviation} + 3.1\,\text{Focal distance} * \text{Deviation} \quad (4)$$

As shown in Fig. 11, increasing the power of laser from 200 to 450 W significantly augmented the welded samples' tensile strength from 200 to 540 MPa. It could be, therefore, said that increasing the power of laser at the focal distance of 0 mm had the most significant influence on increasing the tensile strength. The increase rate of tensile strength, when the focal distance was increased, gradually diminished due to the reduction in the depth of laser beam penetration through material thickness. Additionally, it could be said that, variation of focal distance was clearly influential at high laser power, where there was sufficient melt volume. At the low levels of laser power, due to incomplete melting and penetration, no significant variation on tensile strength was observed.

Fig. 12 illustrates the effect of increasing the focal distance at different locations of the laser beam deviated toward both base metals or center of the location of the two workpieces attached to each other. It could be vividly seen that maximum tensile strength was gained at the contact location of the two samples, where the maximum depth of melt pool was created. By the deviation through every base metal, the tensile strength was reduced about 20%, while a significant reduction of about 60% was observed by increasing the

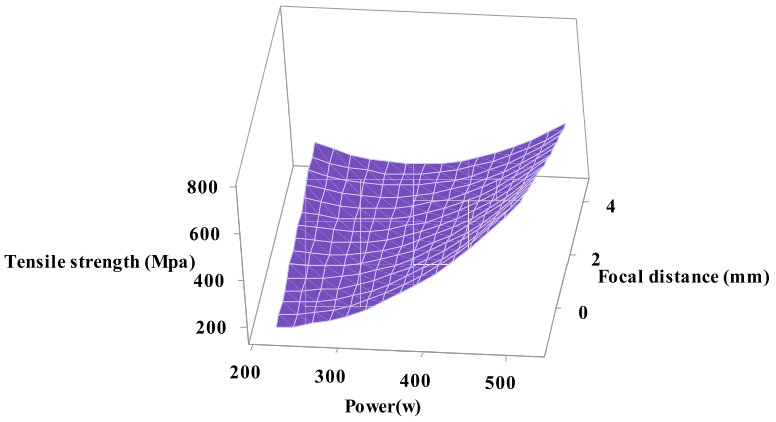

Fig. 11. The impact of focal distance and laser power on the tensile strength of the weld joint.

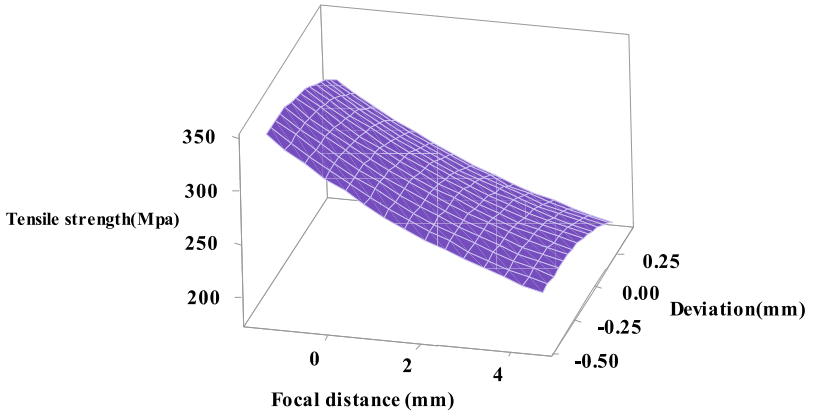

Fig. 12. The impact of the laser beam's deviation and focus distance on the tensile strength of the weld sample.

focal distance to the value of 4 mm. The maximum reduction went to the deviation of Inconel 600 at the focal distance of 4 mm due to the remarkable diminishment of the laser beam energy density according to the lower absorption coefficient of Inconel 600.

Fig. 13 depicts a clear comparison between the impact of laser power and laser beam deviation on the welded joint tensile strength. Clearly, the laser power was the most influential factor on tensile strength. By changing the power of laser from 250 to 450 W, the tensile strength was more than 2.5 folds (the average value of about 550 MPa). On the other hand, it could be clearly observed that laser beam deviation did not evidently change the variation of tensile strength, as compared to the laser power. The variation of tensile strength had a nonlinear trend and the slope of increasing the tensile strength was sharply increased after the laser power level of 400 W due to the significant augmentation of the melt pool depth.

4.1.5. The impact of laser device parameters on the weld joint elongation

The most influential factors on the elongation of the welded samples were laser power and the focal distance, according to the ANOVA results, as presented in Table 9. Rsq = 87.44% and Lack of fit = 0.358 showed that the model of regression could be well fitted with the experimental data. The equation of elongation regression (5) was composed of nonlinear and linear terms.

$$\begin{aligned}\text{Elongation}\,(\%) = {} & -6.39 + 0.04781\,\text{Power} - 0.00836\,\text{Speed} + 0.54\,\text{Focal distance} - 6.0\,\text{Deviation} - 0.206\,\text{Focal distance} * \text{Focal distance} \\ & - 6.87\,\text{Deviation} * \text{Deviation} - 0.00428\,\text{Power} * \text{Focal distance} + 0.0129\,\text{Power} * \text{Deviation} + 0.00321\,\text{Speed} * \\ & \text{Focal distance} - 0.0097\,\text{Speed} * \text{Deviation} + 1.90\,\text{Focal distance} * \text{Deviation}\end{aligned} \tag{5}$$

Fig. 14 illustrates variation in the elongation of the welded samples. In general, increasing the focal distance significantly reduced the elongation to about one third in case the laser beam deviated toward Inconel 600. At the focal distance of 0 mm, laser beam was deviation toward duplex steel, which clearly reduced the elongation rate; meanwhile, at the focal distance of 4 mm, deviation of laser beam to the duplex steel gradually increased the elongation rate. It could be, therefore, concluded that at the focal point of 4 mm, the absorption of Inconel 600 was reduced and therefore, the rate of elongation, according to the lower depth of the melt pool, was significantly decreased. At the focal point of 0 mm, there was also enough penetration of melt pool and therefore, the elongation reached to the highest value. From Inconel 600 to the duplex steel, the elongation rate was gradually decreased due to the clear

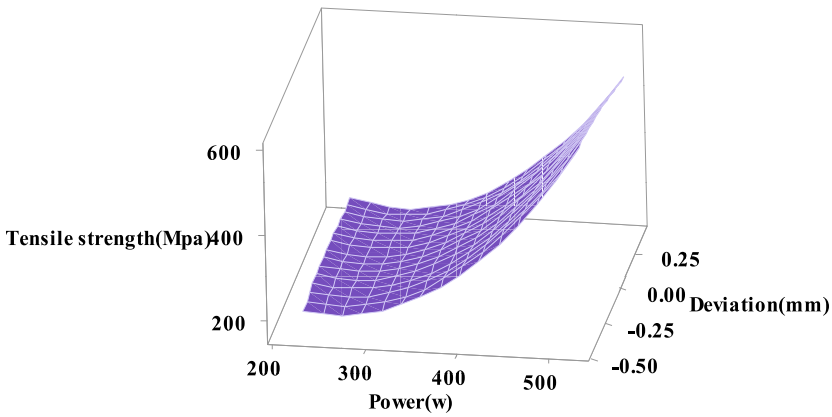

Fig. 13. The power of laser and laser beam deviation impact on the tensile strength of the weld joint.

Table 9
ANOVA results for elongation.

Source	DF	Adj SS	Adj MS	F-Value	P-Value
Model	11	283.829	25.803	10.13	0.000
Linear	4	252.565	63.141	24.79	0.000
Power (W)	1	212.901	212.901	83.58	0.000
Speed (mm/min)	1	2.769	2.769	1.09	0.313
Focal distance (mm)	1	25.347	25.347	9.95	0.006
Deviation (mm)	1	1.333	1.333	0.52	0.480
Square	2	7.127	3.564	1.40	0.275
Focal distance (mm)*Focal distance (mm)	1	5.886	5.886	2.31	0.148
Deviation (mm)*Deviation (mm)	1	2.080	2.080	0.82	0.380
2-Way Interaction	5	9.176	1.835	0.72	0.618
Power (W)*Focal distance (mm)	1	3.286	3.286	1.29	0.273
Power (W)*Deviation (mm)	1	0.533	0.533	0.21	0.653
Speed (mm/min)*Focal distance (mm)	1	3.286	3.286	1.29	0.273
Speed (mm/min)*Deviation (mm)	1	0.533	0.533	0.21	0.653
Focal distance (mm)*Deviation (mm)	1	4.588	4.588	1.80	0.198
Error	16	40.758	2.547		
Lack-of-Fit	12	33.558	2.796	1.55	0.358
Pure Error	4	7.200	1.800		
Total	27	324.587			
S R-sq R-sq (adj) R-sq (pred)					
1.59605 87.44% 78.81% 50.34%					

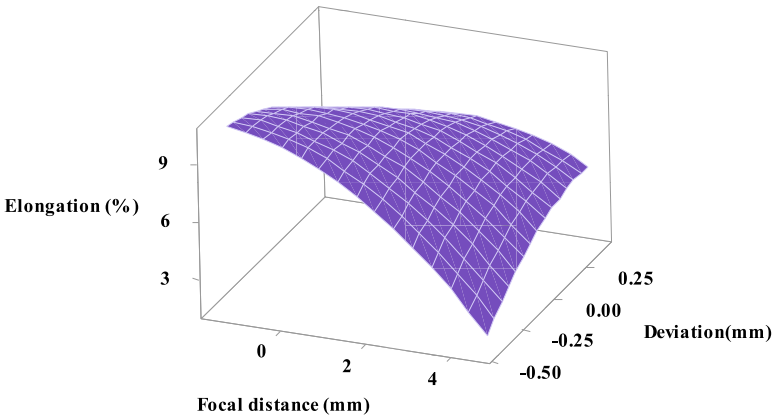

Fig. 14. The impact of focal distance and laser beam deviation on elongation of the weld sample.

reduction of the Inconel 600 melt volume. Therefore, it could be said that the elongation rate of the welded samples had remarkable sensitivity that was related to the melted volume of Inconel 600 participation at the fusion zone.

Fig. 15 depicts the laser power and beam deviation impacts on the elongation rate of the welded samples. By changing the power of the device from 250 to 450 W, the elongation of the welded samples showed a three-fold increase due to creating a higher depth of the melt pool and higher temperature gradient. Additionally, laser beam deviation toward duplex stainless steel slightly increased the elongation rate, as compared to that of Inconel 600. It could be said that high energy density of the laser beams by the augmentation of laser power not only fully penetrated through the workpiece thickness, but also extended the weld width; therefore, the effect of the melted volume of both metals on extending the laser beam deviation toward DSS did not alter the melt volume of Inconel 600. Hence, by the deviation of laser beam toward duplex steel, the elongation rate of the welded samples was not decreased, particularly at a high laser power level more than 400 W.

Fig. 16 shows the impact of welding speed and focal distance on the elongation of the welded samples. By increasing the welding speed from 200 mm/min to 450 mm/min, the elongation rate was reduced about 50%. At the low welding speed of 200 mm/min, increasing the focal distance permanently decreased the elongation rate. At the high welding speed, with increasing the focal distance from 0 to 2 mm, the elongation rate was raised due to creating a higher melt volume. With further increase of focal distance from 2 to 4 mm, due to the reduction in the penetration rate of laser beam, the energy density and therefore, elongation rate were decreased.

By examining the results obtained above and comparing them with the previous ones, as well as studying the previous sources in numerical methods such as machine learning, it could be concluded that the use of numerical methods in material and manufacturing

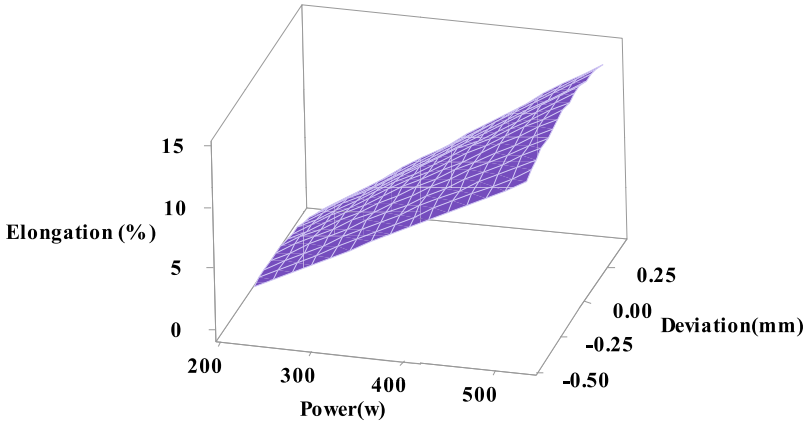

Fig. 15. The impact of laser beam deviation and laser power on elongation of the weld sections.

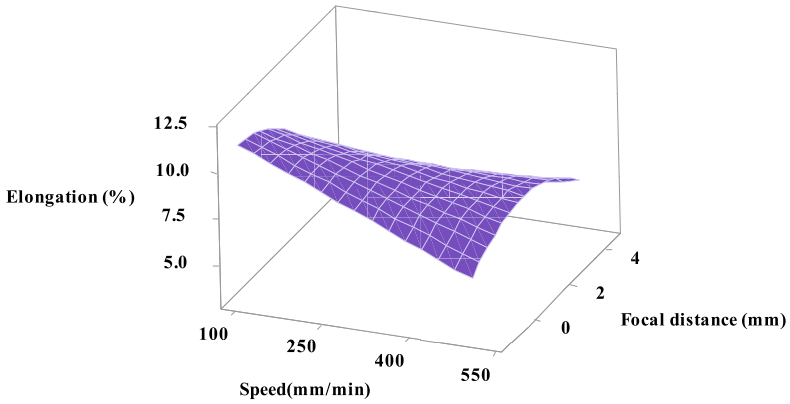

Fig. 16. The impact of scanning speed and focal distance on the elongation of the joints.

engineering is very different [31,32]. By comparing these results and the experimental ones, and considering their good agreement, we can also highlight the importance of simultaneously using experimental and numerical studies.

4.2. Microstructure analysis of dissimilar weld

Investigation of the microstructure and mechanical properties is very important in manufacturing technologies and material sciences, and some studies have been previously done in this field. By studying these results, one can conduct a better analysis on the state of the base metal [33–35]. The samples were etched with 10% oxalic acid solution under 15 s with 12 DC power supply. The microstructure analysis at different areas from both base substrates to the molten zone was performed by the optical microscope and SEM. By using Energy-dispersive X-ray spectroscopy, the weight percentage of elements at the dendritic and interdendritic areas of the fusion zone and HAZ was analyzed.

Fig. 17 a to 17. f shows the microstructural changes of the weld joint from both base metals to the weld center. Fig. 17 b illustrates the microstructure of the Inconel 600 base metal composed of the austenitic matrix with a considerable number of twins that could be observed in many grain boundaries. The microstructure of DSS base metal included austenite grains at the ferrite matrix (see Fig. 17 f). According to Fig. 17 a and 17. c, adjacent to the DSS base metal, at the molten line, the unmixed zone could be clearly observed because of incomplete dissimilar alloys mixing and the difference in the chemical composition and melting point of duplex steel. Higher melting point of duplex stainless steel, which was about 50 °C, prevented complete melting and alloy composition at the fusion line. At the HAZ region of Inconel 600, a grains growth area could be evidently observed due to the heat input from the fusion zone (see Fig. 17 d). The molten area microstructure of dissimilar section could be observed in Fig. 18. As it is demonstrated in Fig. 17 e and18. b, the fusion zone microstructure at the weld center was composed of a cellular and columnar dendritic structure, showing epitaxial grain growth at different directions. According to the direction of temperature gradient and the melt flow at different regions of the fusion zone, the microstructure pattern was clearly changed (see Fig. 18 a). The temperature gradient direction was highlighted in Fig. 18 a by

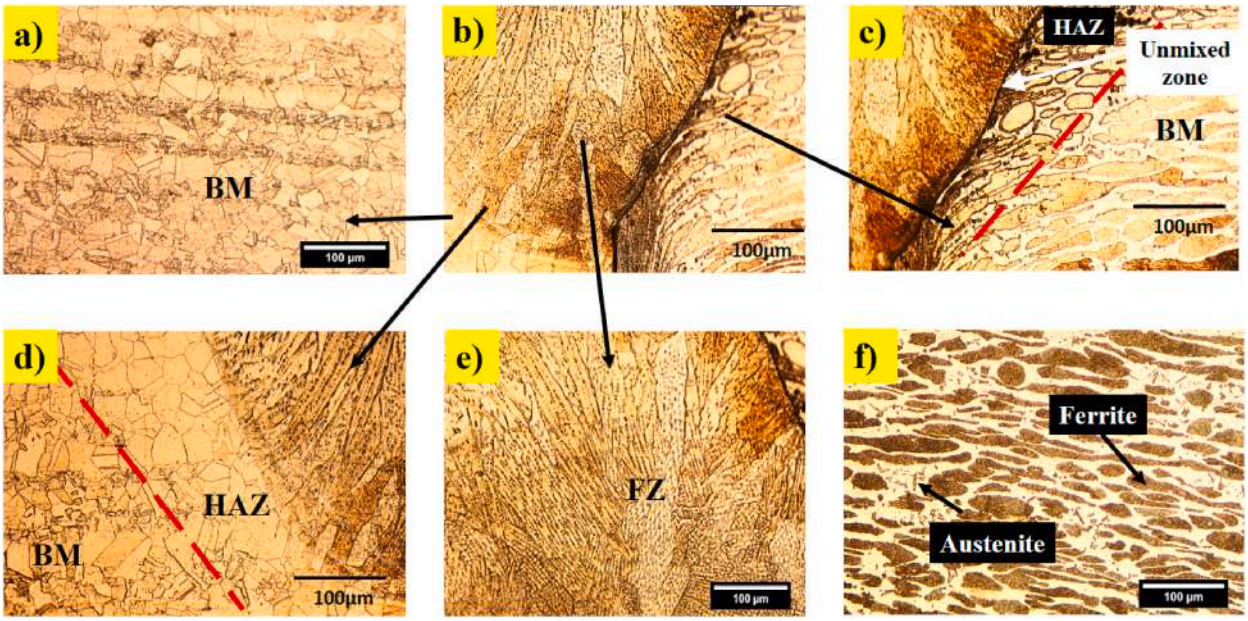

Fig. 17. The weld section microstructure at laser power of 375 W, speed 100 mm/min, focal distance of 1.5 mm, a) Inconel 600 base metal, b) weld joint, c) HAZ duplex, d) HAZ Inconel 600, e) fusion zone, f) duplex base metal.

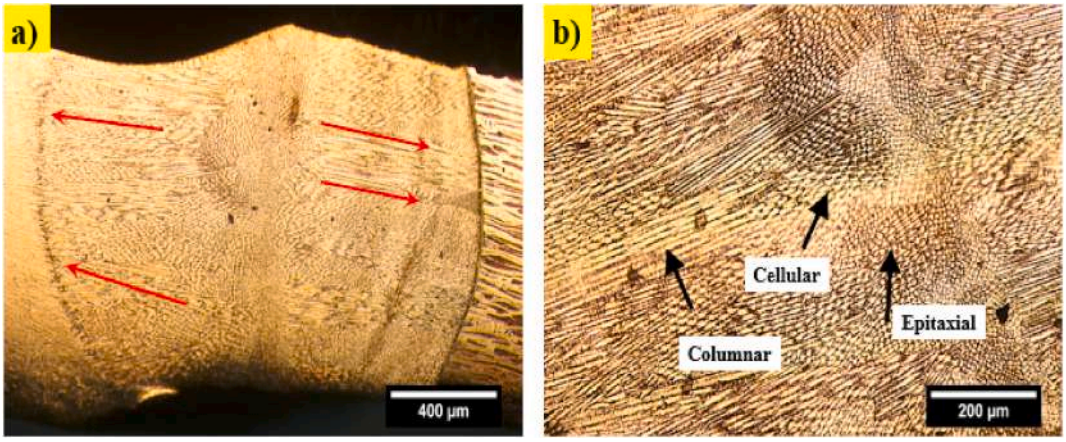

Fig. 18. Weld joint microstructure of a) fusion pool, b) molten zone center.

red arrows as means of a heat transfer symbol toward both base metals. The changes in the solidification mode can generally determine the final microstructure at different locations of the fusion area [21,24].

Fig. 19 shows the weld section microstructure at the power of laser 525 W and velocity of 300 mm/min. Due to the surge in the cooling rate from the molten line to the center of the weld, in comparison to the 375 W power and scanning velocity of 10 mm/min, the dendritic structure varied from the columnar one to a finer cellular one; also, the growth of the grains was observed in a direction perpendicular to the weld zone fusion lines and heat transfer of the HAZ regions [21]. Comparison of the fusion zone microstructure in Fig. 19 e and 18. b shows that finer dendrites created at the higher laser welding speed and faster cooling rate, as reported in Ref. [24].

Additionally, as could be observed from Fig. 20 that, at the lower part of the fusion zone, the solidification grain boundaries (SGBs) could be clearly seen at the weld zone interface to the duplex stainless steel base metal, which was mainly formed by the redistribution of grains and competitive growth during solidification at the boundaries of the melt pool. Fig. 20 b clearly displays that only the duplex stainless steel microstructure at the HAZ had been slightly changed. An evident transformation from ferrite to austenite grains and changes in the direction of the grains at the HAZ region could be observed as a result of heating near the fusion line. At the region near the DSS, the bulk of the microstructure contained cellular dendrites. Therefore, it could be concluded that the unmixed zone could have a notable impact on determining the final distribution of cellular and columnar dendrites at the fusion zone. By considering Fig. 21, it could be noticed that the fusion line was permanently formed at Inconel 600 side because of observing the extended heat affected zone

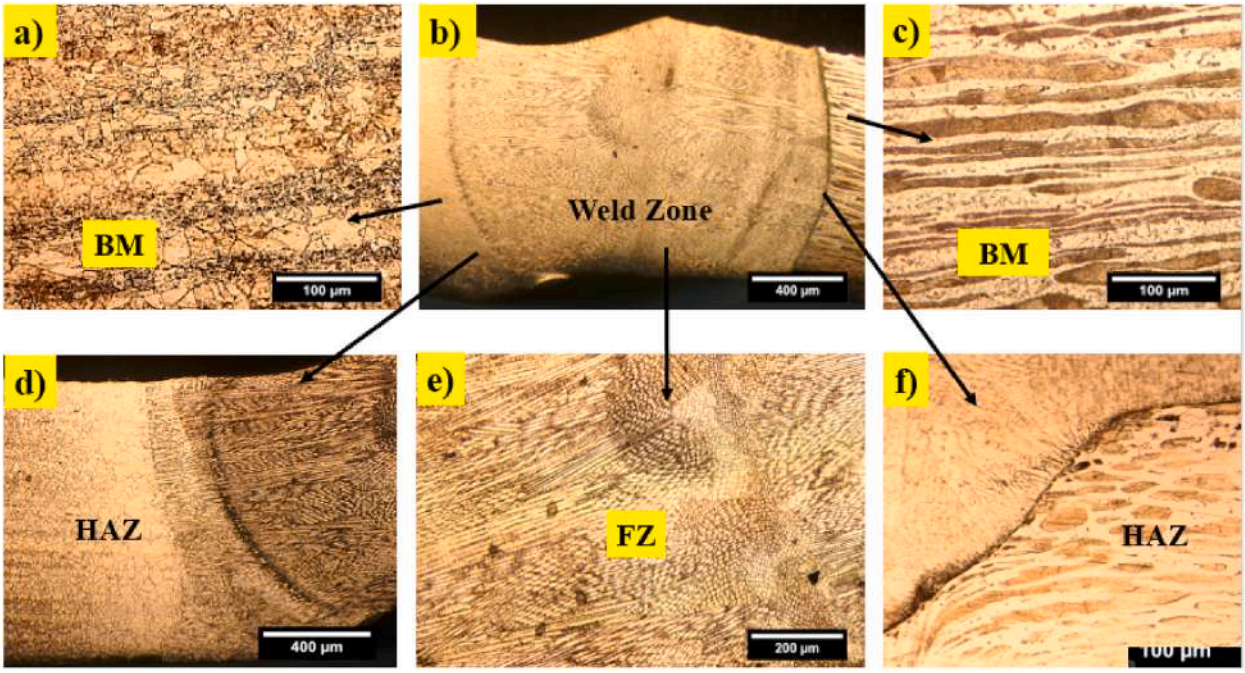

Fig. 19. Microstructure of weld joint at laser power of 525 W, speed 300 mm/min, focal distance of −1.5 mm, a) Inconel 600 base metal, b) weld joint, c) duplex base metal, d) HAZ of Inconel 600, e) fusion zone, f) HAZ duplex.

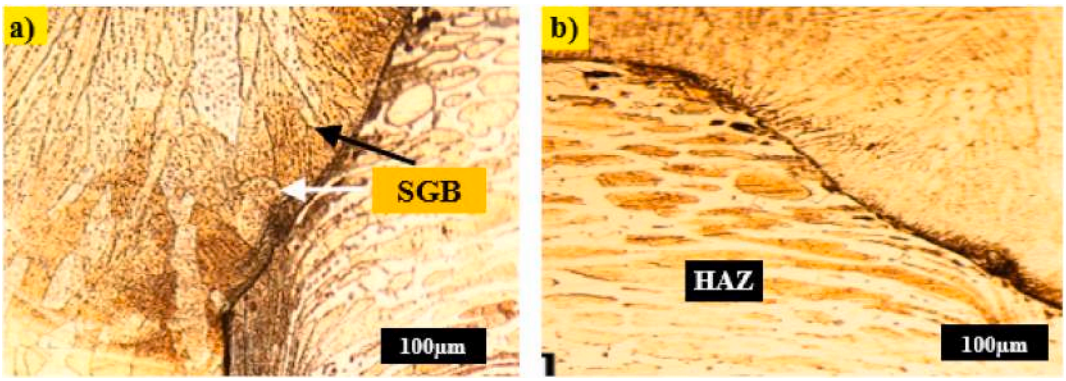

Fig. 20. Microstructure of the weld at a) fusion line inside the melt pool, b) HAZ adjacent to duplex base metal.

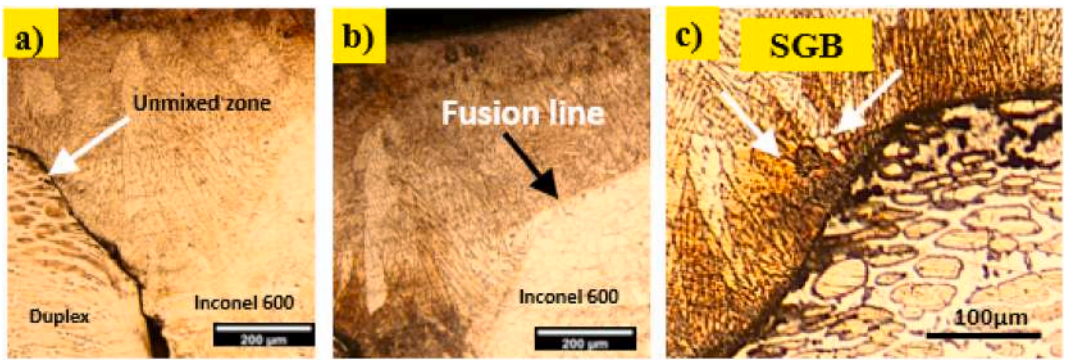

Fig. 21. Microstructure of the weld at a) unmixed zone adjacent to duplex steel, b) HAZ adjacent to Inconel 600 side, c) SGB near duplex fusion line.

at Inconel 600 side. On the other hand, due to higher melting point of duplex stainless steel, the heat affected zone observed at narrow region and only the orientation of grains without microstructural changes was observed. Therefore, at the boundary region of duplex stainless steel side to the fusion zone region, a narrow gap without metallurgical bonding with duplex steel base metal is observed that is known as unmixed zone. The reason behind this could be higher melting point of duplex steel and melting the Inconel 600 majorly by the laser beam. The unmixed zone generally formed at downer portion of workpiece thickness where the laser beam maximum energy density is lower and thereby the melting efficiency is clearly lower. Generally, due to the incomplete mixing of the fusion zone with duplex base metal particularly at low level of laser power and higher melting point of duplex steel, the unmixed zone was formed at duplex steel side. At lower levels of the laser power, the volume of the melted materials and the time for high temperature dissipation significantly reduced and thereby the melting efficiency of duplex steel clearly diminished. Hence the possibility of unmixed zone formation evidently increased. At GTAW welding of Inconel 600 with filler material due to different chemical composition of filler material with Inconel 600, formation of unmixed zone was reported in Ref. [36]. The SGB (solidification grain boundaries) are generally formed at the interface region between solid and melted region boundary due to existing different intensive directional heat transfer rate from solid material (duplex stainless steel). As it is observed in Fig. 21 c, the size, shape and orientation of this grains looks different with other grains at the region adjacent to the duplex stainless steel side.

The SEM images have been taken from different sections, as illustrated in Fig. 22. There were three different types of cellular dendrites (Fig. 22 d), interdendritic microstructure (Fig. 22 c) and columnar dendritic microstructure (Fig. 22 b). According to the variations in the melt flow, temperature gradient and solidification rate from the fusion line to the weld center, the resultant grain growth clearly changed at different areas of the fusion zone.

Fig. 23 depicts the microstructure of dissimilar weld joint at laser power of 375 W from the Inconel 600 base metal to the duplex 2205. The coarsened grains at HAZ region of Inconel 600 is observed at Fig. 23 c. At the fusion zone region, the cellular and inter-dendritic grains are observed at different areas of the fusion zone as shown in Fig. 23 e and f. The austenite grains at the ferrite matrix are observed at the HAZ of duplex stainless steel (see Fig. 23 d).

The EDS analysis at different points of the melt pool, thus, implied that remarkable changes in weight percentage of Ni, Cr and Fe had occurred, as shown in Table 10. Across the width of the fusion zone, the weight percentage of Ni was notably reduced from 50 to 35% weight, while Fe was increased from 16 to 26% from the Inconel 600 to the duplex side. Hence, it could be said that the fusion zone was mainly composed of Ni. Fig. 24 illustrates the line scan analysis results and its position from the weld cross section. As depicted in Fig. 24 b, the EDS line scan analysis resulting from both base alloys to the molten zone confirmed the overall trend of changes in the elemental weight percentage and composition of Fe at the Ni base fusion zone. The weight of Ni dwindled about 30% from the fusion line adjacent to Inconel 600. On the contrary, the weight of Fe was sharply diminished up to 220% and the Cr element

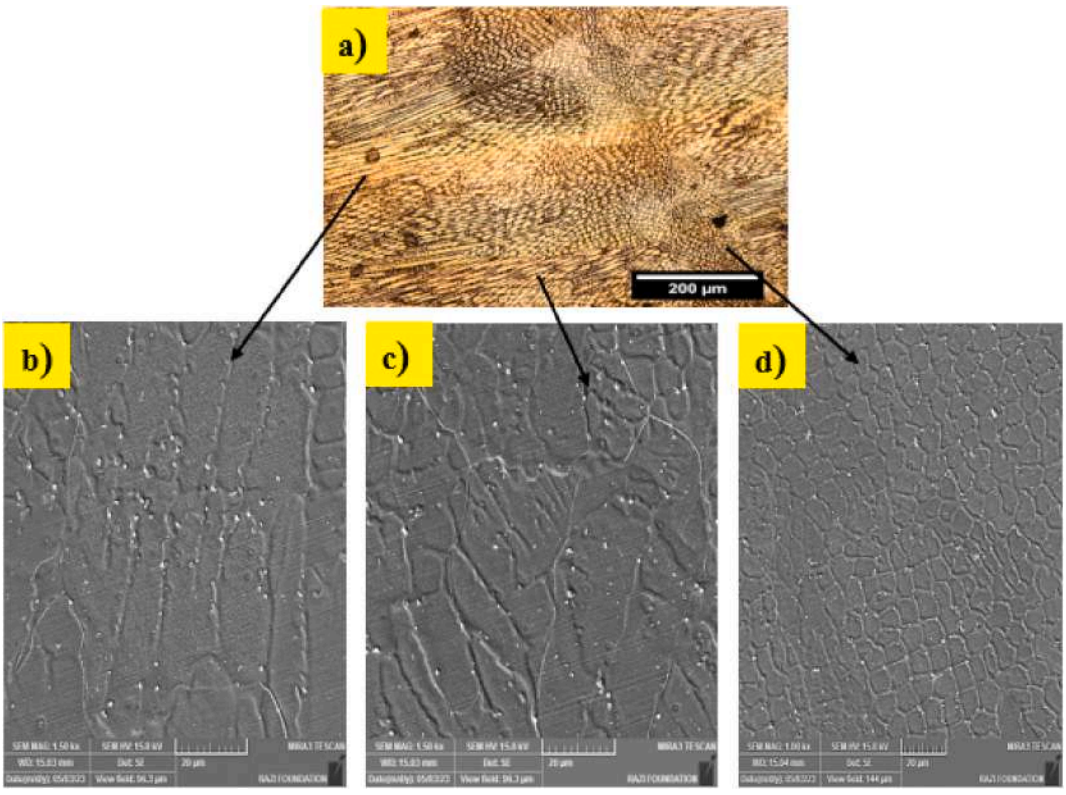

Fig. 22. Microstructure of the fusion zone for a) different location, including b) columnar dendrite, c) interdendritic, d) cellular dendrite.

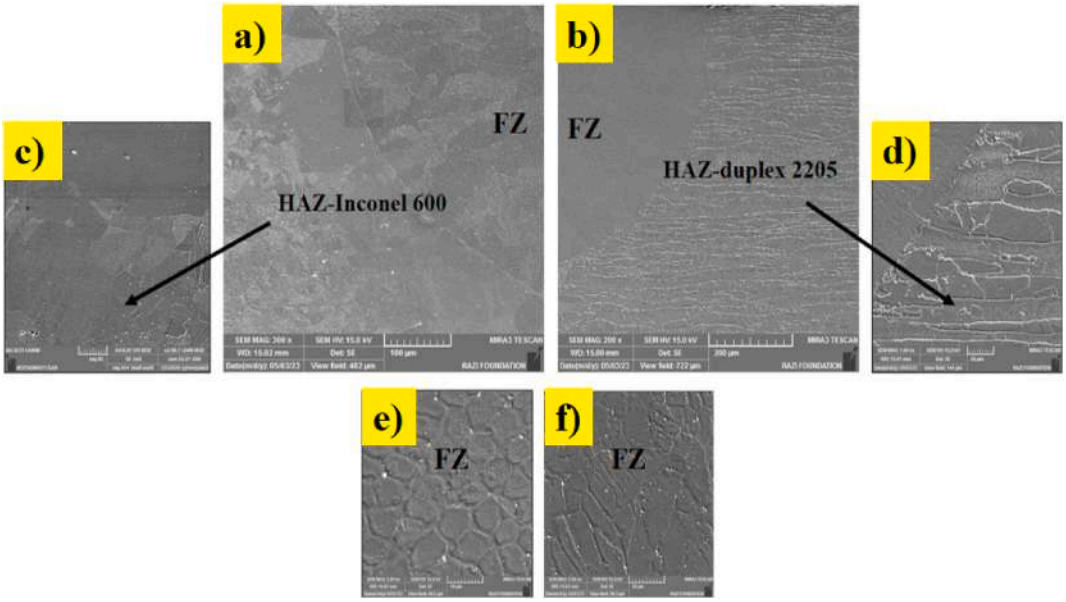

Fig. 23. Microstructure of the fusion zone at laser power of 375W a) Inconel 600 side, b) duplex side c) HAZ Inconel 600 side, d) HAZ duplex side, e) cellular dendrite, f) inter-dendrite microstructure of fusion zone.

Table 10
EDS analysis results at five points of the weld fusion zone from Inconel 600 to the duplex stainless steel.

Element	Si	Cr	Mn	Fe	Ni	Mo	Au
	Weight (%)						
Point 1	0.25	16.39	0.17	22.97	43.25	2.04	14.93
Point 2	0.38	18.37	0.25	26.14	50.15	4.70	–
Point 3	0.68	19.28	–	24.37	43.73	1.30	10.63
Point 4	0.20	13.94	–	16.09	43.69	1.39	24.70
Point 5	0.27	15.02	–	19.50	37.83	1.97	25.42

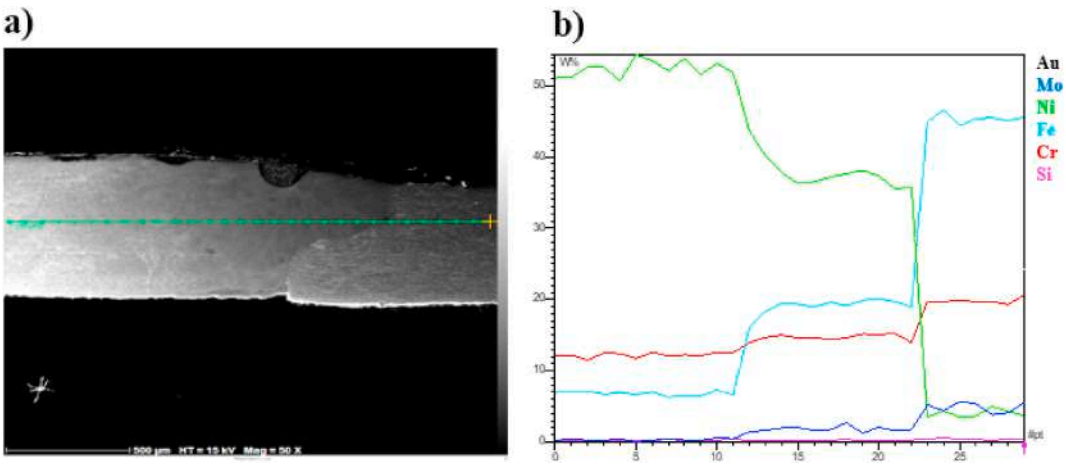

Fig. 24. Line scan EDS analysis of weld joint power of 375 W, speed 300 mm/min for a) weld joint, b) weight percentage graph.

was also decreased about 5% from the duplex steel fusion line. It could be, therefore, concluded that alloy composition had occurred during the formation of the dissimilar fusion zone of both alloys, although the melting participation of duplex stainless steel was limited in comparison to Inconel 600 alloy. Hence, it could be said that the abrupt decrease of Fe and Cr elements at the fusion line of the duplex alloy was related to the unmixed zone of DSS with the molten area. Furthermore, the Cr percentage at the fusion zone almost

remained at the same level of the Inconel 600 base metal.

According to the EDS line scan analysis shown in Fig. 24 b, at the weld fusion zone interface with Inconel 600, the percentage of Ni significantly reduced about 45 percent and the Fe percentage clearly increased. The Mo slightly increased up to 5 percent from Inconel 600 base metal to the fusion zone. On the contrary, at duplex side interface, the Fe percentage remarkably reduced about 40 percent flowed by gradual reduction of Cr and Mo, respectively.

Fig. 25 a shows the points at the HAZ of Inconel 600 (point C, D). The EDS point analysis was performed. As shown in Table 11, the weight percentage of Ni, Cr and Fe was similar to that of the Inconel 600 base metal. It, thus, implied that no changes in elements composition had occurred. On the other hand, points A and B depict the chemical composition of the HAZ region of the duplex stainless steel (see Fig. 25 b). According to Table 11, the points B and A represent austenite and ferrite phases in an orderly state with slight discrepancy in the elemental weight percentage.

4.3. XRD analysis

The XRD analysis, which was taken from the weld metal with the laser beam from sample S1 (J/mm), showed the austenite phase (γ: Ni–Cr–Fe) with chemical formulas $Ni_{2.9}Cr_{0.7}Fe_{0.36}$ and $Cr_{0.19}Fe_{0.7}Ni_{0.11}$ and the formation of laves $(Cr, Ni, Fe)_2(Mo, Nb$ and $Ti)$ as reported in Ref. [37]. Fig. 26 shows the different phases obtained for sample S1 in the indicated peaks. Laves phases can be deduced from S1 peaks in XRD analysis. During the joining process by laser beam welding, phase analysis showed the presence of austenite phase (γ: Ni–Cr–Fe) and lavas in the weld metal created.

4.4. Weld bead appearance

Fig. 27 shows the image of the weld bead appearance of the laser welded samples at different welding speeds. By decreasing welding speed, the width of the weld bead increased significantly. Also, the overlap of weld bead surface evidently reduced when the welding speed increased. A clear reduction of weld bead width is observed when the welding speed increased (see Fig. 27 a and b). The appearance of the weld bead shows that the melting participation of Inconel 600 was clearly risen and major part of the weld bead width extended toward Inconel 600 as highlighted in Fig. 27 c. According to the microstructural images from weld fusion zone cross section, it can be concluded that major part of the melted materials volume composed of Inconel 600. Additionally, lower melting point of Inconel 600 creates higher melt volume which in turn has a direct impact on weld bead width and its extension toward Inconel 600. The weld bead overlap effect seems to have more tendency at Inconel part compared to the duplex part. Because of having slower speed of solidification at Inconel part, the pattern of the weld bead overlap seems to be different from Inconel base metal to the duplex side.

4.5. Microhardness analysis of dissimilar weld cross section

The microhardness test was then performed across the weld fusion zone section of the samples with different laser power level. The average microhardness of Inconel 600 was about 300 HV at the base metal. As it is observed in Fig. 28, at the HAZ region of Inconel 600 and welding condition with the power of 525 W, hardness was decreased from the base metal to the molten line due to the existence of coarse grains. From the fusion line of Inconel 600 to the center weld fusion zone, microhardness was clearly increased to the maximum

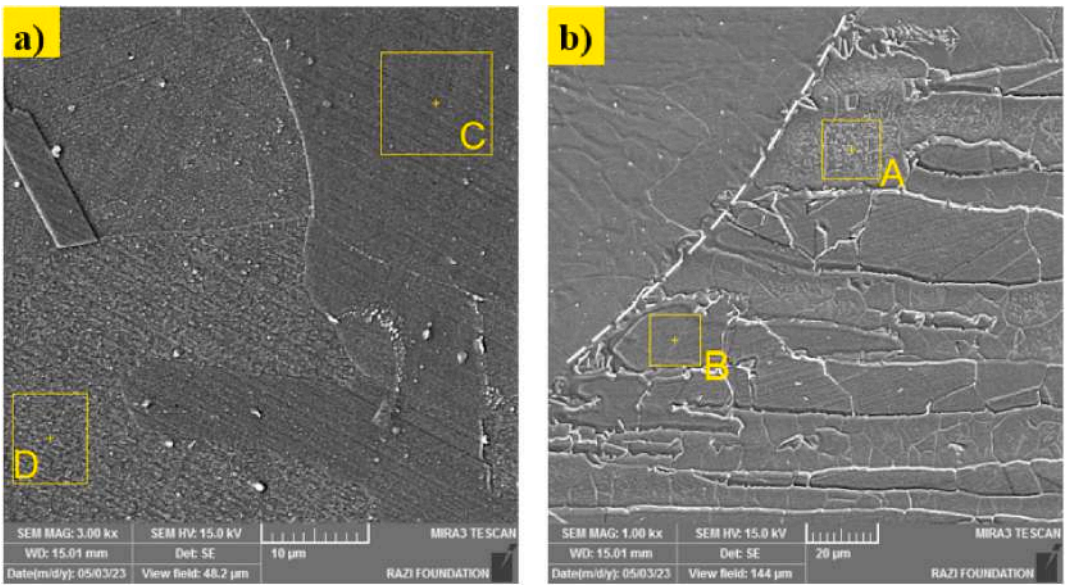

Fig. 25. EDS point analysis for a) Inconel600 HAZ, b) duplex HAZ.

Table 11
EDS analysis results of the points of the HAZ for Inconel 600 and duplex stainless steel.

Element		Al	Si	Cr	Mn	Fe	Ni	Mo
Region	Metal	Weight (%)						
HAZ A	Duplex	0.15	0.58	25.97	–	59.67	5.22	8.41
HAZ B		0.20	0.58	23.60	–	61.24	8.07	6.32
HAZ C	Inconel 600	–	0.44	15.70	0.00	8.66	69.65	5.55
HAZ D		0.23	0.33	15.48	0.00	8.89	70.65	4.41

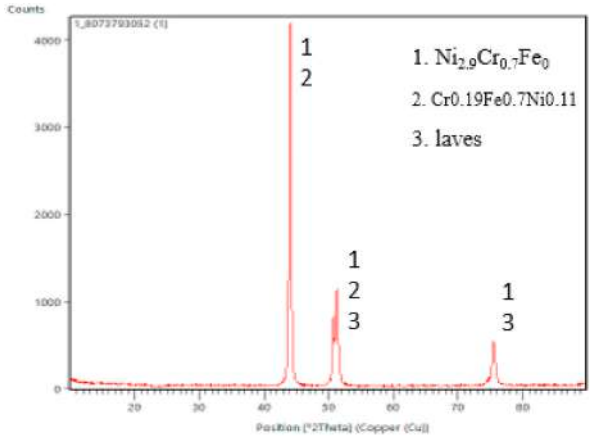

Fig. 26. XRD plots of different phases in the welded sample with laser power of 525 W, speed 300 mm/min, focal distance of −1.5 mm.

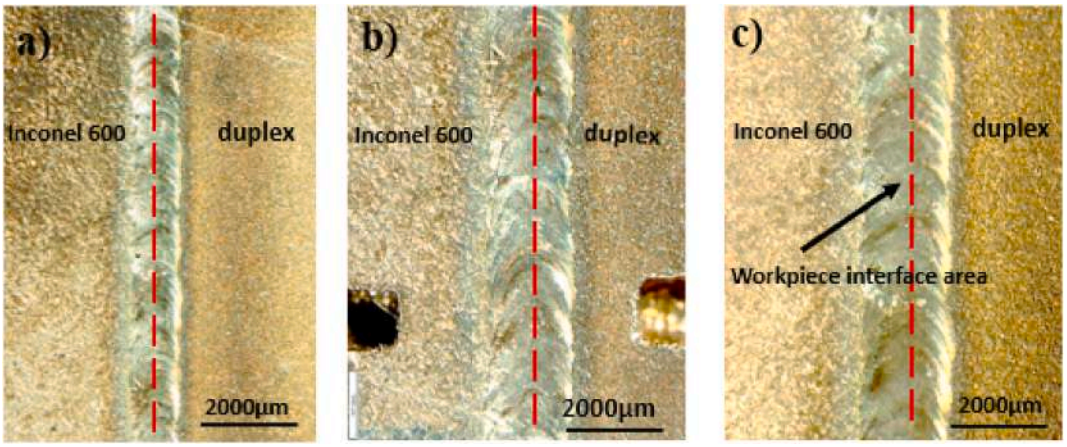

Fig. 27. The weld bead appearance of dissimilar welds of Inconel 600 and duplex steel at laser power of 375 W, beam deviation of 0 mm and welding speeds of a) 500 mm/min, b) 300 mm/min, c) 100 mm/min.

values of 370 and 330 for the laser power of 525 and 375 W, respectively. It could be, therefore, said that higher laser power by considering higher welding speed created steep temperature gradient that ended in finer columnar and cellular grains, which, in turn, had higher hardness, as compared to the laser power of 375 W. At the HAZ region of the duplex stainless steel, because of the variation in the size of austenite grains (bigger grain size), micro hardness was slightly reduced for both samples from the fusion line to the duplex base metal. In general, the variation in microhardness values for welding under the considered conditions (laser power 500W and speed 300 mm/min) was evidently higher due to the existence of more steep temperature gradient, particularly from the Inconel 600 base alloy to the fusion area.

From Inconel 600 toward HAZ, the hardness reduced because of coarsened grain size at this region. From the fusion line of the Inconel 600 toward the center of the fusion zone, the hardness of sample welded at 375 W slightly reduced due to changing the microstructure from columnar dendrite to cellular dendrite. At the center of the fusion zone, the hardness reached to the highest value due to formation different combination of fine cellular grains. From the center of the weld fusion zone toward duplex steel, the

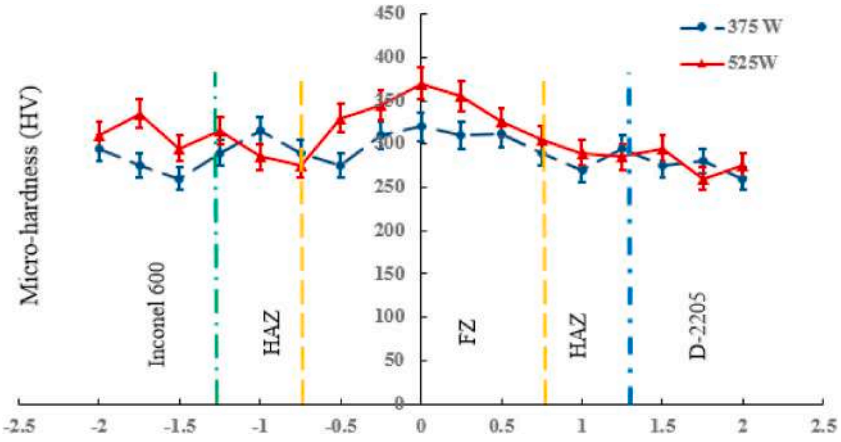

Fig. 28. Microhardness profile across the weld joint from base alloys to the molten zone at distance of 0.4 mm from top surface for welding speed 200 mm/min and powers of laser of 525 W, and 375 W and scanning velocity of 100 mm/min.

hardness gradually reduced due to formation of bigger size cellular grains and slightly increased near the fusion line with duplex steel due to formation of columnar dendrite microstructure.

Fig. 29 illustrates the effect of laser power and welding speed at concavity and convexity of the weld bead profile. As it is observed in Fig. 29 a, at lower laser power of 375 W and slow welding speed of 100 mm/min, the weld bead upper shape has concavity about 0.17 mm due to lower melting volume and higher ablation rate and downward flow of the molten material toward center of the weld bead at low welding speed. On the other hand, at high laser power of 525 W and speed of 400 mm/min depicted in Fig. 29 b, the melt volume incredibly increased up to the full thickness of the material and the weld bead upper part shape has had convexity about 0.21 mm. Hence, it can be concluded that using higher laser power created more melt volume without notable ablation at higher welding speed which in turn resulted in convex weld bead shape.

4.6. Tensile characterization of the dissimilar welded sections

As mentioned in sections 4.1.4 and 4.1.5, the laser power and focal distance had a great effect on the elongation and tensile strength of the welded sections. Tensile tests were then conducted at the velocity of 3 mm/min on the universal tensile test machine and the samples were welded for 1 time from one side of the samples. All experiments were repeated three times and the average results were reported. Regarding the conditions, the laser power was 450W, the welding scanning velocity was 200 mm/min, and the focal distance was 0 mm (at the focal position on the sample surface), where the welded samples' maximum tensile strength was found. In this situation, the maximum tensile strength of 506 MPa and 21 percent elongation were achieved. Seemingly, because of welding from one side, the melt volume was not sufficient, so that samples showed failure from the base metal of the duplex 2205 stainless steel; its UTS was about 621 MPa. Fig. 30 demonstrates the appearance of the detached tensile tests sections. At this condition, the sample, as depicted in Fig. 30 b, showed failure from the fusion zone. By increasing the focal distance, not only the samples had lower elongation and tensile strength, the failure of the samples could be clearly seen to be adjacent to the fusion line of DSS, as shown in Fig. 30 c and d. No remarkable melted materials were, however, observed, as shown in Fig. 30 d, thus revealing that focal distance was increased about

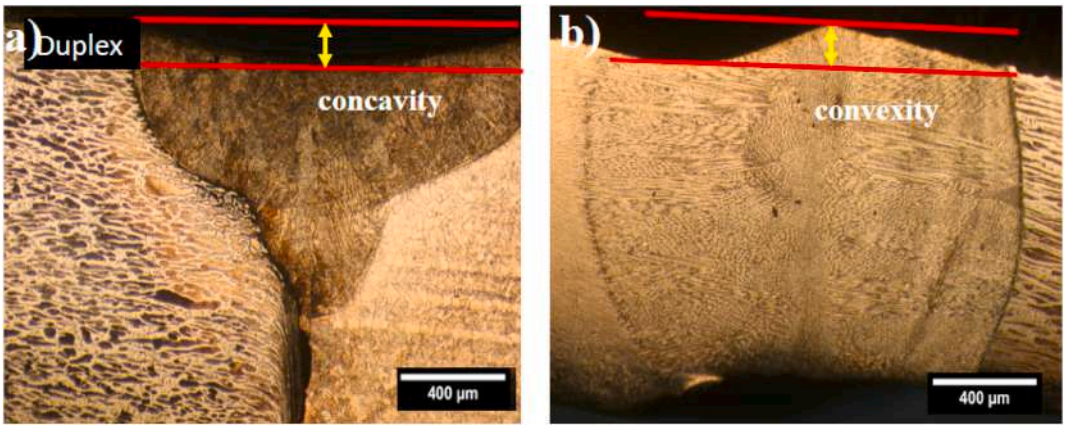

Fig. 29. Appearance of weld surface shape for a) concavity, b) convexity.

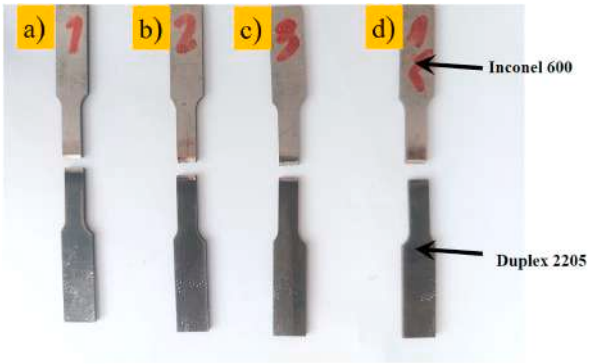

Fig. 30. Tensile tests samples failure appearance of for Exp. No. a)2, b)1, c)23, d)20.

3 mm and the laser power was 300 W. Due to the significant reduction of laser energy density and therefore, the depth of the melt pool, the sample had failure from the unmixed zone adjacent to the fusion line of duplex stainless steel. Moreover, the higher melting point of duplex stainless steel decreased its participation to form the fusion zone and increased the possibility of unmixed zone formation because of having the lower energy level of laser beam. The cross section images of the failure samples from the tensile tests can be observed in Fig. 31. All of the samples had failure from the fusion zone. As it can be clearly observed, the failure section of the samples, as shown in Fig. 31 a and b, seemed to have a more brittle mode and shallower cavities on the Inconel 600 side. The other part of the duplex stainless steel side (Fig. 31 e and h) had small dimples with bigger cavities, although the fracture mode was near the brittle one. The section of Inconel 600 side, as can be seen from Fig. 31 b and c, showed a more ductile mode with more deep dimples and core and cavities. On the other hand, the fracture section of duplex steel, as shown in Fig. 31 f and g, displayed a ductile mode with the biggest dimples and cavities among all samples. The big cracks could be clearly observed in Fig. 31 f. Therefore, the higher laser energy density at the focal distance of 0 mm could produce higher strength and change the mode of fracture from a brittle one to a ductile one with deeper cavities. Compared to the Inconel 600 side, more crack and cavities could be observed at the DSS side section due to the lower mechanical strength. As it was observed in Fig. 31 b, and 19, apart from full weld penetration among material thickness, formation of fine dendritic grains observed in the microstructure of the fusion zone facilitated the occurrence of dislocations and precipitates pinning phenomena during the tensile tests that improved the sample tensile strength among others as obtained in Ref. [38]. As it is evidently observed in Table 12 and Fig. 31 c and d, the samples failure from the fusion zone adjacent to the duplex stainless steel side. From EDS results of Table 11 and Fig. 24 b and EDS phase analysis, due to the solubility of Mo and thereby creating Mo rich phases formed at the inter-dendritic region resulting in loss of ductility and tensile strength. It can be concluded that fracture happens at the fusion zone that laves phases was observed at that region according to the XRD phase analysis as reported in Ref. [20].

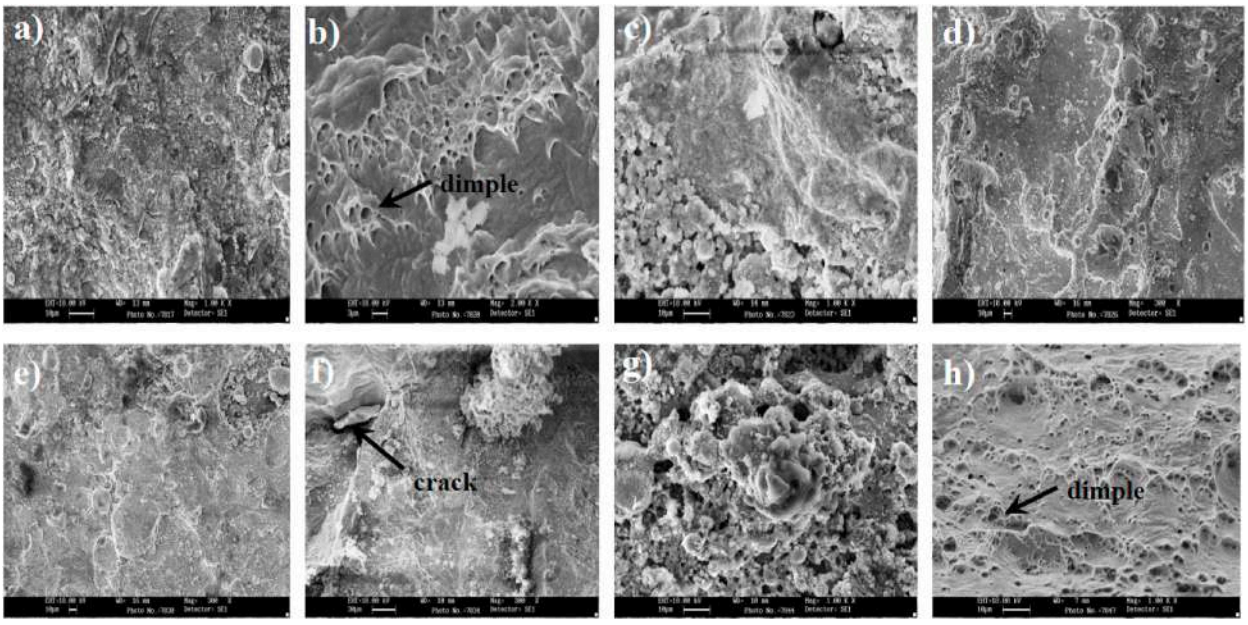

Fig. 31. Weld samples fracture appearance of tensile tests samples for Inconel 600 side for Exp. No. of a) 2, b) 1, c)23, d)20, for duplex stainless steel side for Exp. No. of a) 2, b)1, c)23, d)20.

Table 12
The relation between the tensile strength results and the location of samples fracture.

Sample	Power (W)	Focal distance (mm)	Tensile strength	fracture location	Elongation (%)
S1 (No. 2)	400	0	490	Fusion zone toward duplex	12
S2 (No. 1)	400	3	580	Fusion zone	15
S3 (No. 23)	200	0	320	Duplex HAZ	9
S4 (No. 20)	200	3	250	Duplex fusion line	6

The tensile samples test results presented in Table 12. By reducing laser power from 580 W to 250 W, the tensile strength of the joint significantly reduced. Also the elongation of the tensile tests highly dependent on the laser power level. Another point of tensile tests results was the location of the welded samples fracture. At high laser power levels, the samples fractured from fusion zone while at lower laser powers below 350 W, the samples fractured from the HAZ and the areas adjacent to the duplex steel fusion line. Although both of the base metal have similar material properties, the microstructural changes at the region near the weld fusion line determine the location of fracture.

5. Conclusion

Dissimilar laser welding of DSS 2205 and Inconel 600 was conducted via the CCD experimental design to model the effect of welding parameters on the temperature field near the fusion zone on both metals, melt zone depth, the fusion zone microstructural changes and weld joint mechanical properties.

F0B7 Two parameters of laser power and welding speed had the greatest impact on the depth of the molten area. By transferring the laser beam to the center of the Inconel 600 joint and duplex stainless steel and increasing the laser power from 250 to 450 W, the depth of the molten pool was increased from 0.2 to 1.5 mm.

F0B7 The unmixed zone formed adjacent to the molten line of the DSS, had a notable impact on determining the final distribution of cellular and columnar dendrites at the fusion zone.

F0B7 The EDS line scan analysis results obtained from both substrates to the molten zone confirmed that the weight of Ni dwindled about 30% from the fusion line adjacent to Inconel 600 to the fusion zone. At the weld fusion zone interface with Inconel 600 the percentage of Ni significantly reduced about 30 percent and the Fe percentage clearly increased. On the contrary, a duplex side interface, the Fe percentage remarkably reduced about 120% flowed by gradual reduction of Cr and Mo respectively.

F0B7 From the fusion line of the Inconel 600 toward the center of the fusion zone, the hardness of sample slightly reduced due to changing the microstructure from columnar dendrite to cellular dendrite. At the center of the fusion zone, the hardness reached to the highest value due to formation different combination of fine cellular grains. From the center of the weld fusion zone toward duplex steel, the hardness gradually reduced due to formation of bigger size cellular grains.

F0B7 The cross section images of the failure samples from the tensile tests show that the failure section of the sample seemed to have a more ductile mode and shallower cavities on the Inconel 600 side. Meanwhile, the other part of the duplex stainless steel side showed small dimples with bigger cavities, although the fracture mode was near to brittle.

Data availability statement

Data will be made available on request.

CRediT authorship contribution statement

Ahmad Soleimani: Writing – original draft, Formal analysis. **Mohammad Akbari:** Supervision. **Arash Karimipour:** Methodology, Investigation. **Amir Homayoon Meghdadi Isfahani:** Resources, Methodology. **Reza Nosouhi:** Data curation, Conceptualization.

Declaration of competing interest

The authors declare that they have no known competing financial interests or personal relationships that could have appeared to influence the work reported in this paper.

References

[1] M. Asmael, A. Memarzadeh, A review on recent achievements and challenges in Electrochemical machining of tungsten carbide, Archives of Advanced Engineering Science (2023 May 10) 1–23.

[2] O. Shekoofa, J. Wang, D. Li, Fabrication of N-type nanocrystalline silicon thin-film by magnetron sputtering and antimony induced crystallization, Arch.Adv. Eng. Sci. (2023) 1–11. Jun 16.

[3] H. Taherdoost, M. Madanchian, Analytic Network Process (ANP) Method: A Comprehensive Review of Applications, Advantages, and Limitations, J. Data Sci. Intell. Syst. 1 (1) (2023 May 16) 12–18.

[4] Y. Aghayar, A.R. Naghashzadeh, M. Atapour, An assessment of microstructure and mechanical properties of inconel 601/304 stainless steel dissimilar weld, Vacuum 184 (2021) 109970, https://doi.org/10.1016/j.vacuum.2020.109970.

[5] M. Tümer, T. Mert, T. Karahan, Investigation of microstructure, mechanical, and corrosion behavior of nickel-based alloy 625/duplex stainless steel UNS S32205 dissimilar weldments using ERNiCrMo-3 filler metal, Weld. World 65 (2021) 171–182, https://doi.org/10.1007/s40194-020-01011-0.

[6] G. Sayiram, N. Arivazhagan, Microstructural characterization of dissimilar welds between incoloy 800H and 321 austenitic stainless steel, Mater. Char. 102 (2015) 180–188, https://doi.org/10.1016/j.matchar.2015.03.006.

[7] P. Hididis, M. Nicolaescu, C. Codrean, D. Buzdugan, I.V. Simiti, V.A. Serban, Comparative study between solid state welding and radiant energy welding processes for joining metallic glassy ribbons, Annals of "Dunarea de Jos" University of Galati. Fascicle XII, Welding Equipment and Technology 32 (2021 Dec 31) 71–76.

[8] X.U. Zhiwu, L.I. Zhengwei, L.I. Jianguang, J.I. Wei, Y.A. Jiuchun, Ultrasonic welding process of CF/PPS with thermal radiant preheating and the fracture of welded joint, Trans. China Weld. Inst. 38 (3) (2017) 121–124.

[9] M. Azari, E. Rasti, M.H. Dehkordi, H. Azimy, A. Zarei, S.A. Bagherzadeh, Investigation of temperature distribution and melt pool microstructure in laser fusion welding of Inconel 625 superalloy, J. Laser Appl. 33 (2) (2021 May 1).

[10] T. Baidridge, G. Poling, E. Foroozmehr, R. Kovacevic, T. Metz, V. Kadekar, M.C. Gupta, Laser cladding of Inconel 690 on Inconel 600 super alloy for corrosion protection in nuclear applications, Opt Laser. Eng. 51 (2013) 180–184, https://doi.org/10.1016/j.optlaseng.2012.08.006.

[11] Jae Do Kwon, Dae Kyu Park, Seung Wan Woo, Dong Hwan Yoon, Ilsup Chung, Astudy on fretting fatigue life for the Inconel alloy 600 at high temperature, Nucl. Eng. Des. 240 (2010) 2521–2527, https://doi.org/10.1016/j.nucengdes.2010.05.013.

[12] W. Muhammad, K. Hussain, A. Tauquir, A. ul Haq, A.Q. Khan, Evaluation of Halide-Activated pack boriding of Inconel 722, Metall. Mater. Trans., 30(3), pp. 670–675. https://doi.org/10.1007/s11661-999-0059-z.

[13] Kassim S. Al-Rubaie, Leonardo B. Godefroid, Jadir A.M. Lopes, Statistical modeling of fatigue crack growth rate in Inconel alloy 600, Int. J. Fatig. 29 (2007) 931–940, https://doi.org/10.1016/j.ijfatigue.2006.07.013.

[14] J. Verma, R.V. Taiwade, Effect of welding processes and conditions on the microstructure, mechanical properties and corrosion resistance of duplex stainless steel weldments—a review, J. Manuf. Process. 25 (2017) 134–152, https://doi.org/10.1016/j.jmapro.2016.11.003.

[15] H. Shah Hosseini, M. Shamanian, A. Kermanpur, Characterization of microstructures and mechanical properties of Inconel 617/310 stainless steel dissimilar welds, Mater. Char. 62 (2011) 425–431, https://doi.org/10.1016/j.matchar.2011.02.003.

[16] F. Hejripour, D.K. Aidun, Consumable selection for arc welding between stainless steel 410 and inconel 718, J. Mater. Process. Technol. 245 (2017) 287–299, https://doi.org/10.1016/j.jmatprotec.2017.02.013.

[17] M. Tumer, T. Karahan, T. Mert, Evaluation of microstructural and mechanical properties of dissimilar Inconel 625 nickel alloy–UNS S32205 duplex stainless steel weldment using MIG welding, Weld. World 64 (2020) 21–35, https://doi.org/10.1007/s40194-019-00825-x.

[18] A. Kourdani, R. Derakhshandeh-Haghighi, Evaluating the properties of dissimilar metal welding between inconel 625 and 316L stainless steel by applying different welding methods and consumables, Metall. Mater. Trans. A Phys. Metall. Mater. Sci. 49 (2018) 1231–1243, https://doi.org/10.1007/s11661-018-4469-7.

[19] K. Devendranath Ramkumar, R. Sridhar, S. Periwal, S. Oza, V. Saxena, P. Hidad, N. Arivazhagan, Investigations on the structure – property relationships of electron beam welded Inconel 625 and UNS 32205, Mater. Des. 68 (2015) 158–166, https://doi.org/10.1016/j.matdes.2014.12.032.

[20] G.N. Ahmad, H. Kumar, N.K. Singh, Microstructure and mechanical characterization of laser welded dissimilar joint of DSS 2205 and inconel 625 sheets, AIP Conf. Proc. 2273 (2020), https://doi.org/10.1063/5.0024251, 0–6.

[21] S. Srikanth, A. Parthiban, Microstructural analysis of Nd:YAG laser welding for Inconel alloy, Mater. Today Proc. 21 (2020) 568–571.

[22] K. D.R, D. Sidharth, P.P. Phani, R. Rajendran, K. G.M, S. Narayanan, Microstructure and properties of inconel 718 and AISI 416 laser welded joints, J. Mater. Process. Technol. 266 (2019) 52–62, https://doi.org/10.1016/j.jmatprotec.2018.10.039.

[23] G. Li, J. Huang, Y. Wu, An investigation on microstructure and properties of dissimilar welded Inconel 625 and SUS 304 using high-power CO 2 laser, Int. J. Adv. Manuf. Technol. 76 (2014) 1203–1214, https://doi.org/10.1007/s00170-014-6349-7.

[24] Gulshad Nawaz Ahmad, et al., Investigating the effect of process parameters on weld pool thermal history and mechanical properties of laser welded Inconel 625 and Duplex stainless steel 2205 dissimilar welds, Optik 248 (2021) 168134.

[25] M. Shamanian, M. Valehi, SzpunarJ. KangazianJ, EBSD characterization of the L-605 Co-based alloy welds processed by pulsed Nd:YAG laser welding, Opt. Laser Technol. 128 (2020) 106256.

[26] Maurício David M. das Neves, André Lotto, José Roberto Berretta, Wagner de Rossi, Nilson Dias V. Júnior, Microstructure development in Nd:YAG laser welding of AISI 304 and Inconel 600, Weld. Int. 24 (Issue 10) (2010).

[27] L. Yan, J.E. Jam, M.H. Beni, M.J. Kholoud, D. Baleanu, M. Eskandari Shahraki, Ferial Ghaemi, Effect of laser welding parameters on the temperature distribution, microstructure and mechanical properties of dissimilar weld joint of Inconel 625 and stainless steel 304, Int. Commun. Heat Mass Tran. 131 (2022) 105859.

[28] ASM Handbook Volume 2: Properties and Selection: Nonferrous Alloys and Special-Purpose Materials, ASM International, 1990.

[29] M.J. Rawa, M.H. Dehkordi, M.J. Kholoud, N.H. Abu-Hamdeh, H. Azimy, Using the numerical simulation and artificial neural network (ANN) to evaluate temperature distribution in pulsed laser welding of different alloys, Eng. Appl. Artif. Intell. 126 (2023 Nov 1) 107025.

[30] C. Sun, M.H. Dehkordi, M.J. Kholoud, H. Azimy, Z. Li, Systematic evaluation of pulsed laser parameters effect on temperature distribution in dissimilar laser welding: a numerical simulation and artificial neural network, Opt Laser. Technol. 163 (2023 Aug 1) 109407.

[31] H. Gaur, B. Khidhir, R.K. Manchiryal, Solution of structural mechanic's problems by machine learning, International Journal of Hydromechatronics 5 (1) (2022) 22–43.

[32] B. Liu, W. Lu, Surrogate models in machine learning for computational stochastic multi-scale modelling in composite materials design, International Journal of Hydromechatronics 5 (4) (2022) 336–365.

[33] N. Erum, J. Ahmad, Structural, elastic and mechanical properties of cubic perovskite materials, Archives of Advanced Engineering Science (2023 Jun 5) 1–9.

[34] L. Gang, G. Huang, H. Yuan, S. Xia, W. Tan, Analysis and optimisation of impact wear of diesel engine needle valve assembly, International Journal of Hydromechatronics 5 (1) (2022) 80–91.

[35] Y. Yongbin, S.A. Bagherzadeh, H. Azimy, M. Akbari, A. Karimipour, Comparison of the artificial neural network model prediction and the experimental results for cutting region temperature and surface roughness in laser cutting of AL6061T6 alloy, Infrared Phys. Technol. 108 (2020 Aug 1) 103364.

[36] A. Srikanth, M. Manikandan, Development of welding technique to avoid the sensitization in the alloy 600 by conventional Gas Tungsten Arc Welding method, J. Manuf. Process. 30 (2017 Dec 1) 452–466.

[37] G.N. Ahmad, M.S. Raza, N.K. Singh, H. Kumar, Experimental investigation on Ytterbium fiber laser butt welding of Inconel 625 and Duplex stainless steel 2205 thin sheets, Opt Laser. Technol. 126 (2020 Jun 1) 106117.

[38] K.D. Ramkumar, R. Sridhar, S. Periwal, S. Oza, V. Saxena, P. Hidad, N. Arivazhagan, Investigations on the structure–Property relationships of electron beam welded Inconel 625 and UNS 32205, Mater. Des. 68 (2015 Mar 5) 158–166.